

Application of OMI, SCIAMACHY, and GOME-2 satellite SO₂ retrievals for detection of large emission sources

V. E. Fioletov,¹ C. A. McLinden,¹ N. Krotkov,² K. Yang,^{2,3} D. G. Loyola,⁴ P. Valks,⁴ N. Theys,⁵ M. Van Roozendael,⁵ C. R. Nowlan,⁶ K. Chance,⁷ X. Liu,⁷ C. Lee,⁸ and R. V. Martin^{6,7}

Received 5 April 2013; revised 5 September 2013; accepted 7 September 2013.

[1] Retrievals of sulfur dioxide (SO₂) from space-based spectrometers are in a relatively early stage of development. Factors such as interference between ozone and SO₂ in the retrieval algorithms often lead to errors in the retrieved values. Measurements from the Ozone Monitoring Instrument (OMI), Scanning Imaging Absorption Spectrometer for Atmospheric Chartography (SCIAMACHY), and Global Ozone Monitoring Experiment-2 (GOME-2) satellite sensors, averaged over a period of several years, were used to identify locations with elevated SO₂ values and estimate their emission levels. About 30 such locations, detectable by all three sensors and linked to volcanic and anthropogenic sources, were found after applying low and high spatial frequency filtration designed to reduce noise and bias and to enhance weak signals to SO₂ data from each instrument. Quantitatively, the mean amount of SO₂ in the vicinity of the sources, estimated from the three instruments, is in general agreement. However, its better spatial resolution makes it possible for OMI to detect smaller sources and with additional detail as compared to the other two instruments. Over some regions of China, SCIAMACHY and GOME-2 data show mean SO₂ values that are almost 1.5 times higher than those from OMI, but the suggested spatial filtration technique largely reconciles these differences.

Citation: Fioletov, V. E., et al. (2013), Application of OMI, SCIAMACHY, and GOME-2 satellite SO₂ retrievals for detection of large emission sources, *J. Geophys. Res. Atmos.*, 118, doi:10.1002/jgrd.50826.

1. Introduction

[2] Sulfur dioxide (SO₂) plays an important role in the Earth atmosphere. It forms sulfate aerosols that influence weather and climate [Intergovernmental Panel on Climate Change, 2001], leads to acid deposition through formation of sulfuric acid (H₂SO₄) [e.g., Hutchinson and Whitby, 1977], and poses a direct hazard to public health [e.g., Pope and Dockery, 2006; Longo et al., 2010]. Satellite SO₂

observations have been used to calculate volcanic SO₂ budgets and to monitor plumes from volcanic eruptions [e.g., Krueger et al., 2000; Carn et al., 2003; Rix et al., 2012]. It was also demonstrated that satellite instruments can detect SO₂ signals from anthropogenic sources [e.g., Eisinger and Burrows, 1998; Thomas et al., 2005; Carn et al., 2007; Georgoulas et al., 2009; de Foy et al., 2009; Lee et al., 2011; Nowlan et al., 2011; McLinden et al., 2012] and even monitor changes in emission from these sources [Fioletov et al., 2011]. Likewise, satellite SO₂ data were employed to study the evolution of emissions from China [Witte et al., 2009; Li et al., 2010a, 2010b; Jiang et al., 2012].

[3] SO₂ can be retrieved from satellite measurements in the thermal infrared (IR) and ultraviolet (UV) parts of the spectrum. The former type of measurements employed, for example, by Infrared Atmospheric Sounding Interferometer (IASI) instrument, can be used to trace SO₂ from volcanic eruptions [Karagulian et al., 2010; Clarisse et al., 2012] and transcontinental transport of SO₂ pollutions from China [Clarisse et al., 2011]. Measurements in IR are based on the temperature contrast between the surface and air, and therefore they have reduced sensitivity to the boundary layer. The UV-based measurements are sensitive enough to detect boundary-layer SO₂ [e.g., Krotkov et al., 2006] and therefore are better suited for monitoring of anthropogenic SO₂ sources and non-eruptive gaseous volcanic emissions.

¹Environment Canada, Toronto, Ontario, Canada.

²Laboratory for Atmospheric Chemistry and Dynamics, NASA Goddard Space Flight Center, Greenbelt, Maryland, USA.

³Department of Atmospheric and Oceanic Sciences, University of Maryland, College Park, Maryland, USA.

⁴Deutsches Zentrum für Luft- und Raumfahrt, Wessling, Germany.

⁵Belgian Institute for Space Aeronomy (BIRA-IASB), Brussels, Belgium.

⁶Department of Physics and Atmospheric Science, Dalhousie University, Halifax, Nova Scotia, Canada.

⁷Harvard-Smithsonian Center for Astrophysics, Cambridge, Massachusetts, USA.

⁸National Institute of Meteorological Research, Korea Meteorological Administration, Seoul, South Korea.

Corresponding author: V. E. Fioletov, Environment Canada, 4905 Dufferin Street, Toronto, ON, M3H 5 T4, Canada. (Vitali.Fioletov@ec.gc.ca)

[4] Solar backscattered UV radiances in SO₂ absorption wavelengths shorter than 320 nm are also strongly affected by absorption by stratospheric ozone. While the difference in spectral features of ozone and SO₂ absorption in the UV makes SO₂ measurement possible, the total vertical column density (VCD) of SO₂, even over very large anthropogenic sources, is only on the order of 1–2 Dobson units (DU, where 1 DU is equal to $2.69 \cdot 10^{26}$ molecules km⁻²), whereas typical total column ozone values range between 250 and 400 DU. Given that absolute values of ozone and SO₂ absorption coefficients are comparable, small uncertainties in the ozone retrieval may have a significant impact on SO₂ estimates. Furthermore, instrument artifacts may also introduce spectral features that resemble the SO₂ absorption signal, resulting in biases in the derived SO₂ products, especially if the retrieval is performed using only a small number of wavelengths as in the Ozone Monitoring Instrument (OMI) algorithm [Krotkov *et al.*, 2006]. Both instrument characterizations and satellite SO₂ retrieval algorithms have been improved by the developers, and therefore we can expect a more accurate SO₂ with less biases in future data products. In this study we demonstrate that the presently publicly available satellite data products can be enhanced to identify and extract weak SO₂ signals.

[5] Examples of the impact of ozone can be seen in the mean SO₂ distribution derived from the Ozone Monitoring Instrument (OMI) measurements near 30°N and 30°S, where an abrupt change of 0.5 DU occurs [Lee *et al.*, 2009]. This step-like change is related to an algorithmic switch from tropical to midlatitudinal a priori ozone profiles at these latitudes. Similar problems resulting from the interference between ozone and SO₂ retrievals are known for other satellite instruments/algorithms [e.g., Nowlan *et al.*, 2011] demonstrating that fluctuations in ozone distribution may affect retrieved SO₂, yielding local biases. Fioletov *et al.* [2011] noted that elevated SO₂ levels near point sources occurred over an area with a diameter less than 100 km even for industrial sources with very large emissions. Fluctuations in stratospheric ozone are characterized by much larger distances, 1000–2000 km [Liu *et al.*, 2009]. Therefore, spatial filtration can be used to isolate small-scale fluctuations caused by local SO₂ emission sources.

[6] The past decade has seen three satellite UV instruments capable of detecting near-surface SO₂. The Scanning Imaging Absorption Spectrometer for Atmospheric Chartography (SCIAMACHY), 2002–2012, onboard the ENVISAT satellite has a 30×60 km² pixel size but relatively poor spatial coverage as it requires approximately 6 days for the acquisition of a contiguous global map. The Global Ozone Monitoring Experiment-2 (GOME-2) instrument, 2006 to present, on MetOp-A [Callies *et al.*, 2000] provides almost daily global coverage but has even larger pixel size of 40×80 km². OMI, 2004 to present, on NASA’s Aura spacecraft [Levelt *et al.*, 2006] provides the best horizontal resolution (13×24 km² footprint at nadir) among instruments in its class and near-global daily coverage. Satellite data products used in this study are discussed in section 2.

[7] Even with the higher spatial resolution provided by OMI, most anthropogenic sources produce increased SO₂ concentrations that are detectable only within the collocated space of just one or two ground pixels. Instead of an analysis of individual events, this study employs a pixel-averaging technique in which a large number of individual observations

are used in an attempt to quantify the SO₂ spatial distributions near larger SO₂ emissions sources [Fioletov *et al.*, 2011]. Spatial filtration of satellite measurements of atmospheric pollutants has been used, for example, to detect NO₂ emissions from ships or “ship tracks” [Beirle *et al.*, 2004]. In this study, a similar technique was used to remove local biases and detect point sources of SO₂ emissions. The data analysis procedures for single emission sources are described in section 3 along with several case studies.

[8] Elevated SO₂ levels over China related to the industrial activity is one of the most prominent features of global satellite SO₂ maps (see, e.g., Figure 1 or Lee *et al.* [2009]). Asian emissions of several pollutants, including SO₂, have grown substantially over the last two decades [Streets and Waldhoff, 2000] and represent a significant problem for air quality in China [Zhang *et al.*, 2012]. Asian emissions of SO₂ also have a direct impact on regional air quality in North America [e.g., Park *et al.*, 2004; Heald *et al.*, 2006]. In particular, vanDonkelaar *et al.* [2008] found that more than half of the sulfate measured in the lower troposphere over the Canadian province of British Columbia is due to East Asian sources. A second spatial filtration technique, appropriate for regions of elevated SO₂, was used to study SO₂ over China with its very large number of individual sources (section 4).

2. Data

[9] All three instruments used in this study are nadir-viewing spectrometers that measure backscattered radiation in the near UV, the region used to retrieve SO₂ (roughly 310–330 nm) from Sun-synchronous, low-Earth orbits. Differences are found in their overpass times, spatial and spectral resolutions, sampling, and SO₂ retrieval algorithms. In the case of GOME-2, two different data products based on the same measurements but processed with different algorithms were included in the analysis to see what impact a difference in algorithms may have on presented results, bringing the number of data products discussed in this study to 4.

2.1. GOME-2 German Aerospace Center SO₂ Data Product

[10] GOME-2 on MetOp-A is a scanning spectrometer with a spectral coverage of 240–790 nm and a spectral (full width at half maximum) resolution between 0.26 nm and 0.51 nm. The measurements are taken at around 9:30 local solar time and are available from January 2007. The operational GOME-2 total column SO₂ product version 4.6 is produced by the German Aerospace Center (DLR) in the framework of EUMETSAT’s Satellite Application Facility on Ozone and Atmospheric Chemistry Monitoring (O3M-SAF). Slant column densities of SO₂ are determined using the Differential Optical Absorption Spectroscopy (DOAS) method [Platt, 1994] in the wavelength region between 315 and 326 nm. Input parameters for the DOAS fit include the absorption cross section of SO₂ and the absorption cross sections of interfering gases, ozone and NO₂. A further correction is made in the DOAS fit to account for the ring effect (rotational Raman scattering). An additional empirical interference correction is applied to the SO₂ slant column values to reduce the interference from ozone absorption [Valks and Loyola, 2008; Rix *et al.*, 2012]. Level 2 data available from <http://atmos.eoc.dlr.de/gome2> is used. We will

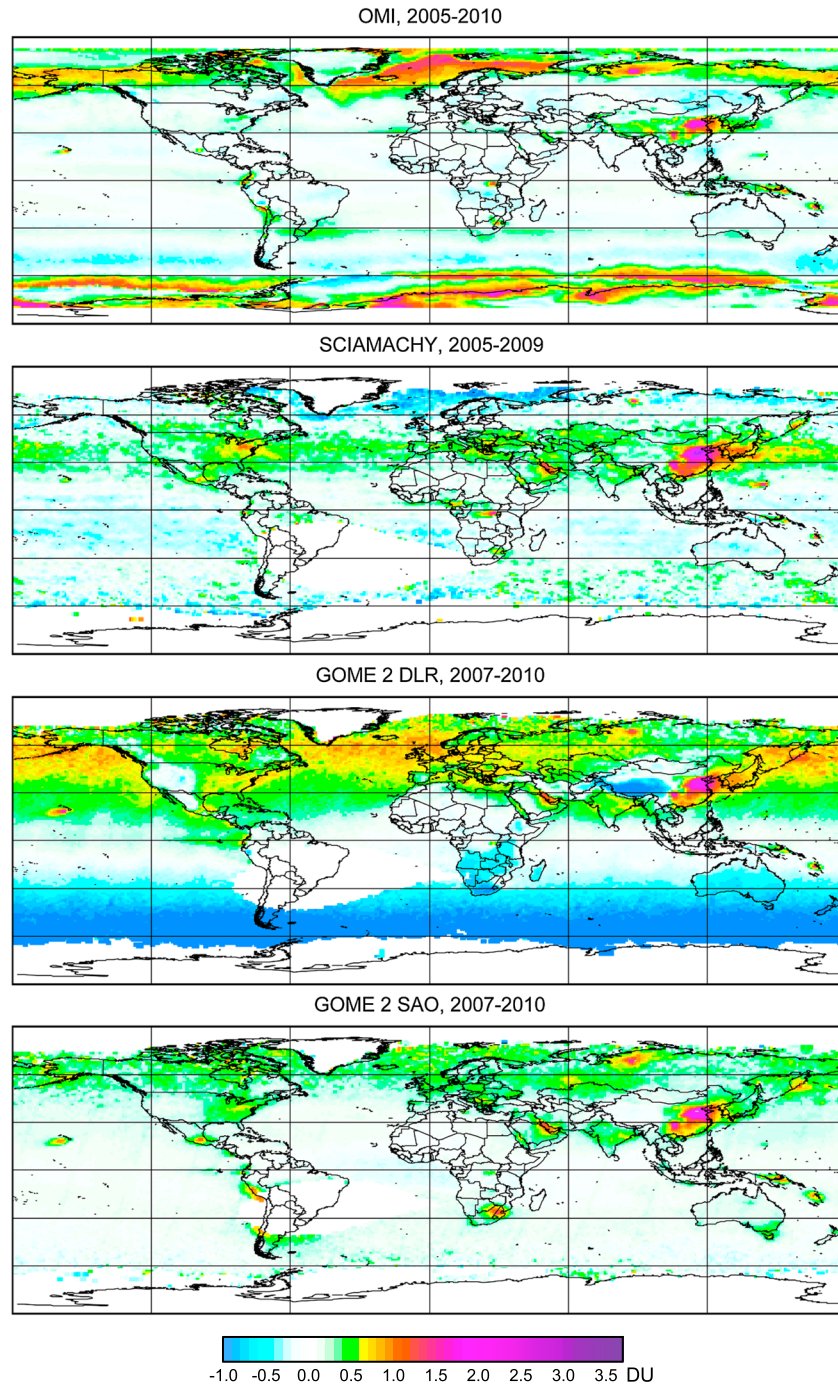


Figure 1. Mean column SO₂ from OMI, SCIAMACHY, and GOME-2 (DLR and SAO versions) data in Dobson units (DU). Note that SCIAMACHY data have a larger bias in 2010 than in other years and for this reason the period was limited to 2005–2009.

refer to this data set as to the GOME-2 DLR data product. It should be also noted that the upcoming GOME-2 DLR version 4.7 data product [Theys *et al.*, 2013] will have smaller biases in background SO₂ values compared to the version 4.6 used in this study.

2.2. GOME-2 Smithsonian Astrophysical Observatory SO₂ Data Product

[11] Another SO₂ data product based on GOME-2 measurements is developed by the Harvard-Smithsonian Center

for Astrophysics, Cambridge, Massachusetts, U.S. [Nowlan *et al.*, 2011]. It uses an optimal estimation approach and combines a full radiative transfer calculation and trace gas climatologies to directly retrieve the vertical column density of SO₂ simultaneously with ozone profile, implicitly including the effects of albedo, clouds, ozone, and SO₂ profiles, and wavelength-dependent air mass factor in the retrieval in the spectral range of 312–330 nm. At the time of this study, data for the period 2007–2010 were available. We will refer to this data set as the GOME-2 Smithsonian Astrophysical

Observatory (SAO) data product. Data can be requested from <http://www.cfa.harvard.edu/atmosphere/>.

2.3. SCIAMACHY SO₂ Data Product

[12] The SCIAMACHY instrument onboard EnviSat measures backscattered radiances between 240 and 2380 nm [Bovensmann *et al.*, 1999]. The Level 2 data product developed by Belgian Institute for Space Aeronomy and available from <http://www.sciamachy.org> is used in this study. Similarly to GOME-2 DLR data product, the retrieval of the SO₂ slant column is done from the spectrum in the wavelength range 315–326 nm using the DOAS technique. The measurements are taken at 10:00 local time. While SCIAMACHY was launched in 2002, these SO₂ data are available from January 2004 to April 2012. It should be noted that other SCIAMACHY SO₂ data products exist [e.g., Lee *et al.*, 2008].

2.4. OMI SO₂ Data Product

[13] The Dutch-Finnish-built Ozone Monitoring Instrument (OMI) [Levell *et al.*, 2006] has been observing aerosols and trace gases, including SO₂, from the NASA EOS Aura satellite platform since 2004 [Schoeberl *et al.*, 2006]. The OMI Band residual Difference (BRD) algorithm makes use of precomputed ozone, Lambertian effective reflectivity, and calibrated residuals at four wavelengths centered on SO₂ absorption bands: 310.8 nm, 311.9 nm, 313.2 nm, and 314.4 nm [Krotkov *et al.*, 2006]. OMI measures 60 cross-track positions (pixels), and the pixel size varies depending on the track position from 13 × 24 km² at nadir to about 28 × 150 km² at the outermost swath angle. Data from the first and last 10 track positions were excluded from the analysis. Thus, only pixels with the across-track pixel width from 24 km to about 40 km were used. The local equator crossing time of Aura is 13:45. Beginning in 2007, some cross track positions corresponding to particular rows in CCD detector were affected by field-of-view blockage and scattered light (called “row anomaly,” see <http://www.knmi.nl/omi/research/product/rowanomaly-background.php>), and these affected pixels were excluded from the analysis. This study focuses on anthropogenic pollution sources that emit SO₂ to the planetary boundary layer (PBL), and therefore a data product specifically designed to represent boundary-layer SO₂ was used [Krotkov *et al.*, 2006]. The data are available from NASA Goddard Earth Sciences Data and Information Services Center: http://disc.sci.gsfc.nasa.gov/Aura/OMI/omso2_v003.shtml. Daily SO₂ and cloud composite images for predefined volcanic regions, eastern China, and Norilsk, Russia are available from <http://so2.gsfc.nasa.gov>.

2.5. Air Mass Factor

[14] The quantity that results from the spectral analysis in each of the datasets described above (except for the GOME-2 SAO product) is the slant column density (SCD), which represents a measure of the total absorption by SO₂ in the measured spectra. In order to convert SCD into the vertical column density (VCD, i.e., total number of molecules in a vertical atmospheric column), the average path of the sunlight through the atmosphere needs to be accounted for. This is done by applying an appropriate column air mass factor (AMF) [Lee *et al.*, 2009] as follows: $VCD = SCD/AMF$.

For SO₂, the AMF is strongly dependent on measurement geometry, surface albedo, clouds, aerosols, ozone, and the shape of the vertical SO₂ profile in the atmosphere. Due to the strong wavelength dependence in ozone absorption and Rayleigh scattering, the AMF is also strongly dependent on the wavelength within the fitting window. In the operational OMI SO₂ boundary layer product a spatially and temporally invariant AMF of 0.36 was used, appropriate for summertime conditions in the eastern U.S. and chosen to represent SO₂ from anthropogenic pollution sources. This constant AMF is also reasonable for the majority of industrial sources located at low elevations in Europe, North America, and China [Krotkov *et al.*, 2008; Lee *et al.*, 2011].

[15] Clearly, detailed AMFs based on local conditions, including a realistic representation of aerosols (which are likely elevated near large pollution sources), are necessary to establish a quantitative link or to expand the analysis to other regions. An alternative is to use model-based estimates of AMFs [e.g., Lee *et al.*, 2011], but this too has shortcomings. If a certain source is not included in the emission inventory used by a model (examples of which are shown below), the AMF values will likely be overestimated since the model would underestimate the fraction of the column in the boundary layer. Moreover, it is unclear if estimates, obtained from the current generation of global air quality model simulations at ~200 km resolution, are representative within several kilometers of the emission site. Based on these considerations, the invariant AMF is applied to the SCIAMACHY and GOME-2 slant column densities.

[16] The choice of OMI wavelengths (310–315 nm) in the BRD algorithm optimizes the instrument sensitivity to weak SO₂ signals in the boundary layer, at the expense of smaller signal-to-noise ratio and reduced UV penetration (smaller AMF). The SCIAMACHY and GOME-2 algorithms are focused on strong volcanic signals and use the DOAS technique at slightly longer wavelengths. In the spectral region 310–330 nm used in the satellite retrievals, the AMF itself increases with wavelength. The difference in the spectral intervals between BRD and DOAS algorithms introduces about 20% bias if the OMI global constant AMF = 0.36 is used. To account for this, AMF = 0.36 was used for OMI and AMF = 0.43 was used for SCIAMACHY and GOME-2 data products. Unlike the other products which determine a SCD, the SAO algorithm obtains the VCD directly. To facilitate comparisons with the other products, the SAO-VCDs are converted to SCDs using the AMFs included with the data product and then AMF = 0.43 was applied to obtain VCD. This approach means it is likely that some input information used in the direct inversion (such as the Goddard Earth Observing System Global 3-D Chemical transport model (GEOS-CHEM) profiles) is not completely eliminated from the SCD by the application of the AMF calculated at a single wavelength.

[17] Thus, all VCD satellite data sets discussed here were based on constant AMFs (0.36 for OMI and 0.43 for the two other instruments). For the purposes of data comparisons of the three instruments and for studying long-term evolution of SO₂ near large sources, the assumption of a constant AMF is acceptable. Once the information presented here is incorporated into emission inventories, however, the use of site-specific AMFs based on model profiles would become the favored approach.

2.6. Data Filtering

[18] To avoid issues related to the data quality and differences in observation conditions between different satellites, data were filtered based on consistent criteria. Only clear-sky data, defined as having a cloud radiative fraction less than 20%, were used. To exclude cases of transient volcanic SO₂, the range of analyzed values were limited to a maximum of 15 DU. Furthermore, to avoid uncertainties related to seasonal dependence of various factors, such as difference in solar zenith angles between the satellites, variable surface albedo (snow), higher ozone optical depth, etc., winter data were excluded from some analyses as discussed in the text. In addition, measurements taken at the solar zenith angles greater than 60° were excluded from the analysis. It appears that measurements from all three instruments after 2010 have been affected by various instrumental degradation problems resulting in higher noise and more frequent erroneous values. For this reason, the main results presented here are based on data for the period up to and including 2010.

2.7. Global SO₂ Distribution

[19] The mean, long-term distribution of SO₂ over the globe estimated using the four satellite data products is shown in Figure 1. Calculations were performed on a 1° by 1° grid using a constant AMF value (0.36 for OMI and 0.43 for the two other instruments). Some features are common on all maps, e.g., elevated SO₂ over China as well as over several active volcanoes, etc. However, the “background” levels, i.e., values over the areas with no obvious SO₂ sources, can be very different. For example, OMI and GOME-2 DLR show mean values of about 1 DU over the Northern Atlantic, north of 60°, while SCIAMACHY mean values are negative (about -1 DU). At northern midlatitudes, SCIAMACHY data show elevated VCDs, by about 0.5 DU, and GOME-2 DLR mean values are even higher, while OMI data do not show any large biases there (except over China). Systematic errors in retrieved background SO₂ resulting from imperfect instrument calibration as well as from, for example, forward model simplifications were substantially suppressed in the present OMI algorithm by empirical residual corrections [Yang *et al.*, 2007]. Nonetheless, Figure 1 shows that some large-scale biases, likely caused by the interference between ozone and SO₂ retrievals, remain in OMI. The GOME-2 SAO product is produced from radiances corrected for a latitude-dependent SO₂ offset using slant columns derived from VCD retrievals over the clean Pacific [Nowlan *et al.*, 2011]. The GOME-2 SAO data product demonstrates smaller biases than the GOME-2 DLR, although SO₂ values over northern midlatitudes, e.g., over Canada, appear to be somewhat elevated. All of this suggests that there are artificial local biases in all satellite data sets that should be removed before the data are used for practical applications.

3. Point Emission Sources: Spatial Smoothing and Local Bias Correction

[20] The pixel-averaging or oversampling approach was applied to analyze the long-term mean spatial SO₂ distribution near an identified source [Fioletov *et al.*, 2011; Streets *et al.*, 2013]. For this, a geographical grid is established around the source and the average of all satellite pixels

centered within a several kilometer radius from each grid point is calculated. Thus, this procedure provides a detailed “subpixel-resolution” spatial distribution of long-term mean SO₂ value in the vicinity of the source. The choice of averaging radius determines the degree of smoothing: averaging with a large radius reduces the noise, but it also reduces the spatial resolution. Due to relatively small OMI pixel size, reliable estimates can often be obtained for smoothing radiuses of 18 km and even smaller. For much larger SCIAMACHY and GOME-2 pixels, larger radiuses (50 km or more) are required. Spatial smoothing with a 60 km radius was applied to all four satellite data sets for the sake of consistency.

[21] As discussed in section 2, there are substantial local biases in the satellite data. This is further illustrated in Figure 2, where SO₂ data (smoothed with a 60 km radius) near two sources, a cluster of power plants in South Africa and the Mount Etna volcano, Italy, are shown. As the original data demonstrate, local biases magnitude can be comparable with the mean SO₂ values for some data products. Since these biases appear as large-scale patterns, they can be removed with a spatial high-pass filter. To accomplish this, SO₂ values from pixels centered between 250 km and 300 km from the source location were averaged and this average value (or local bias) was subtracted from all measurements near the source. It was also found that these local biases vary from month to month, thereby necessitating monthly local bias correction. Mean SO₂ values around similar sources corrected in this manner are very similar as illustrated by Figure 2.

[22] Smoothed in the same way (with 60 km radius) and with the local bias removed, data from the four data products show much better agreement in SO₂ distributions in the vicinity of the point sources than noncorrected data. Moreover, they also show similar temporal changes in SO₂ values as illustrated by Figure 3 where data for two volcanic sources, Anatahan and Kilauea, are shown. Recall that contributions from explosive volcanic emissions were largely removed by the 15 DU cutoff limit imposed on the data. Each sensor shows a decrease in average SO₂ by a factor of 2–3 between 2005–2007 and 2008–2010 for Anatahan volcano, while values near Kilauea increased threefold. This increase in emissions from Kilauea in 2008 led to health problems in the Hawaiian population [Longo *et al.*, 2010].

[23] Anthropogenic sources also can produce high long-term mean SO₂ values detectable by all three satellite instruments. Copper and nickel smelters at Norilsk in northern Russia (70°N, 88°E), shown in Figure 1, comprise probably the largest industrial SO₂ “point” source. Its reported emission level was about 2000 kT yr⁻¹ in the late 2000s [Norilsk Nickel, 2009]. Independent estimates based on aircraft measurements in 2010 estimate its annual emissions at about 1000 kT yr⁻¹ [Walter *et al.*, 2012]. With the local bias removed, all three satellite instruments (and four data products) reported mean average values of 2–2.5 DU at Norilsk for summer months (May–August). A cluster of 10 coal-burning power plants near Johannesburg in South Africa with production of more than 1000 MW each form another “hot spot” of elevated SO₂ values likewise seen in data from all four satellite data products (Figure 1).

[24] Another example of an industrial SO₂ source, Cantarell and Ku-Maloob-Zaap Oil Fields in the Gulf of Mexico, is illustrated by Figure 4. This is one of Mexico’s largest

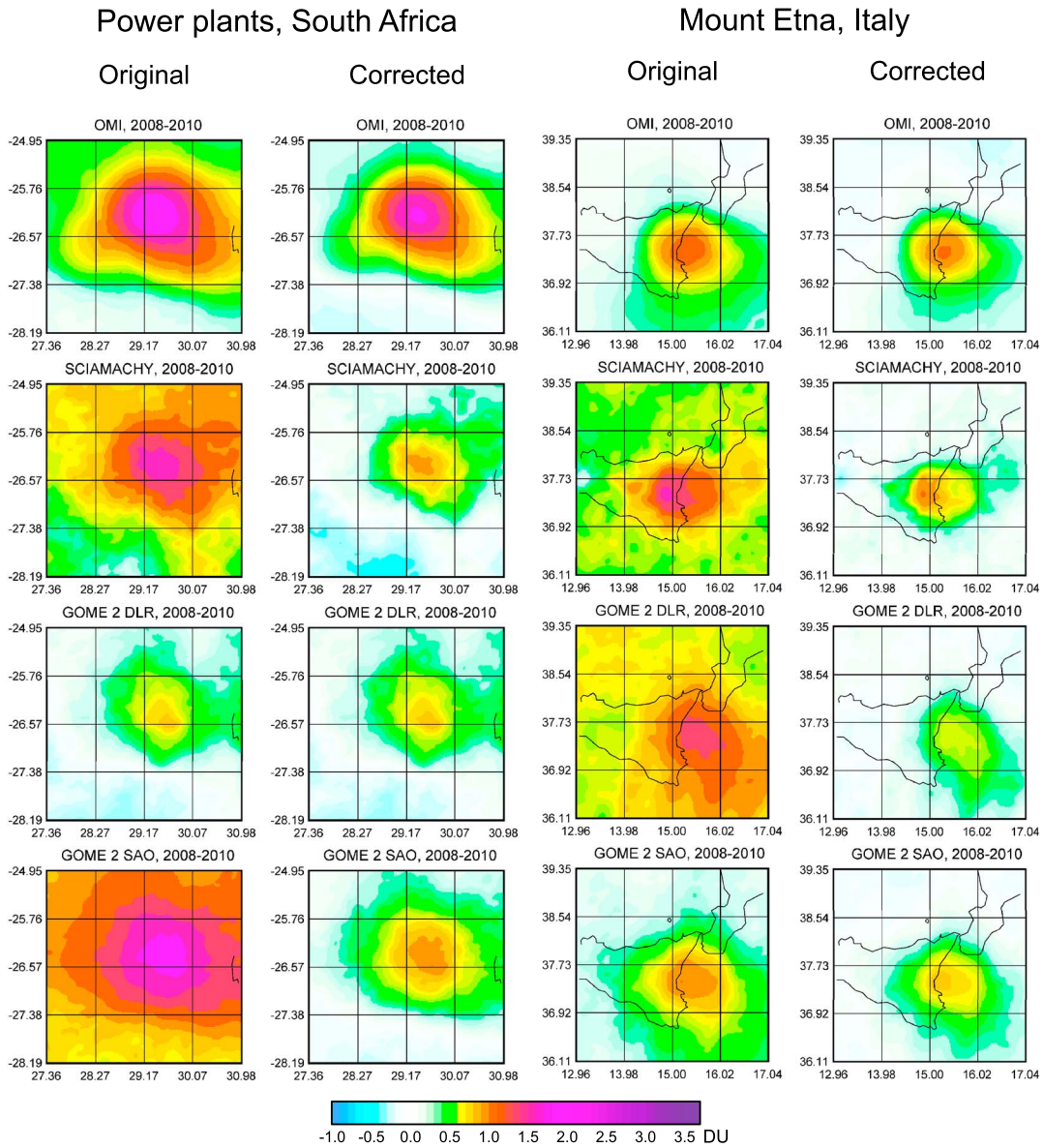


Figure 2. Mean SO₂ values (in DU) over a cluster of power plants near Johannesburg, South Africa, and the Mount Etna volcano, Italy, estimated for four data products. Data are smoothed using the averaging radius of 60 km as described in the text. Original data as well as data with the local bias removed are shown.

oil-producing regions with more than 200 oil wells in operation [Aquino *et al.*, 2005; Feller, 2012]. According to Figure 4, all four data sets demonstrate a substantial increase in SO₂ signal in recent years. The oil production from the Cantarell field is declining, and in order to compensate for this decline production from Ku-Maloob-Zaap is increasing. However, oil in the Ku-Maloob-Zaap is heavier, i.e., with higher sulfur content, than in the Cantarell field [Talwani, 2011] and thus probably yield a higher SO₂ output in recent years, consistent with that seen by the satellites. Little information is available about SO₂ emissions from that region. In the late 1990s, SO₂ emission levels were estimated to be about 180 kT yr⁻¹, and at that time 77% of emissions were coming from the Cantarell field [Villasenor *et al.*, 2003]. From the late 1990s to the mid-2000s, the oil production from the Cantarell field nearly doubled and then started to decline. If the emission to production ratio remained

constant during that time, SO₂ emissions were about 350 kT yr⁻¹ in 2005–2007. This case represents an example of a large and growing SO₂ source not included in the most recent emissions inventories according to the Emissions of atmospheric Compounds & Compilation of Ancillary Data (http://eccad.sedoo.fr/eccad_extract_interface/JSF/page_login.jsf) and the widely used EDGAR v4.2 database [Janssens-Maenhout *et al.*, 2011].

[25] The secondary maximum in the southwest corner on the map in Figure 4 is likely related to the Gas Processing Centers’ gas sweetening and sulfur recovery plant at Nuevo Pemex and other oil and gas exploration mining and refinery-related sources in the Tabasco State [Valdés-Manzanilla *et al.*, 2008].

[26] The elevated SO₂ levels discussed in the examples above are well above the noise level. Figure 4 shows the ratios between the mean values and the standard errors of the means,

Anatahan (16°N, 146°E)

Kilauea (19°N, 156°W)

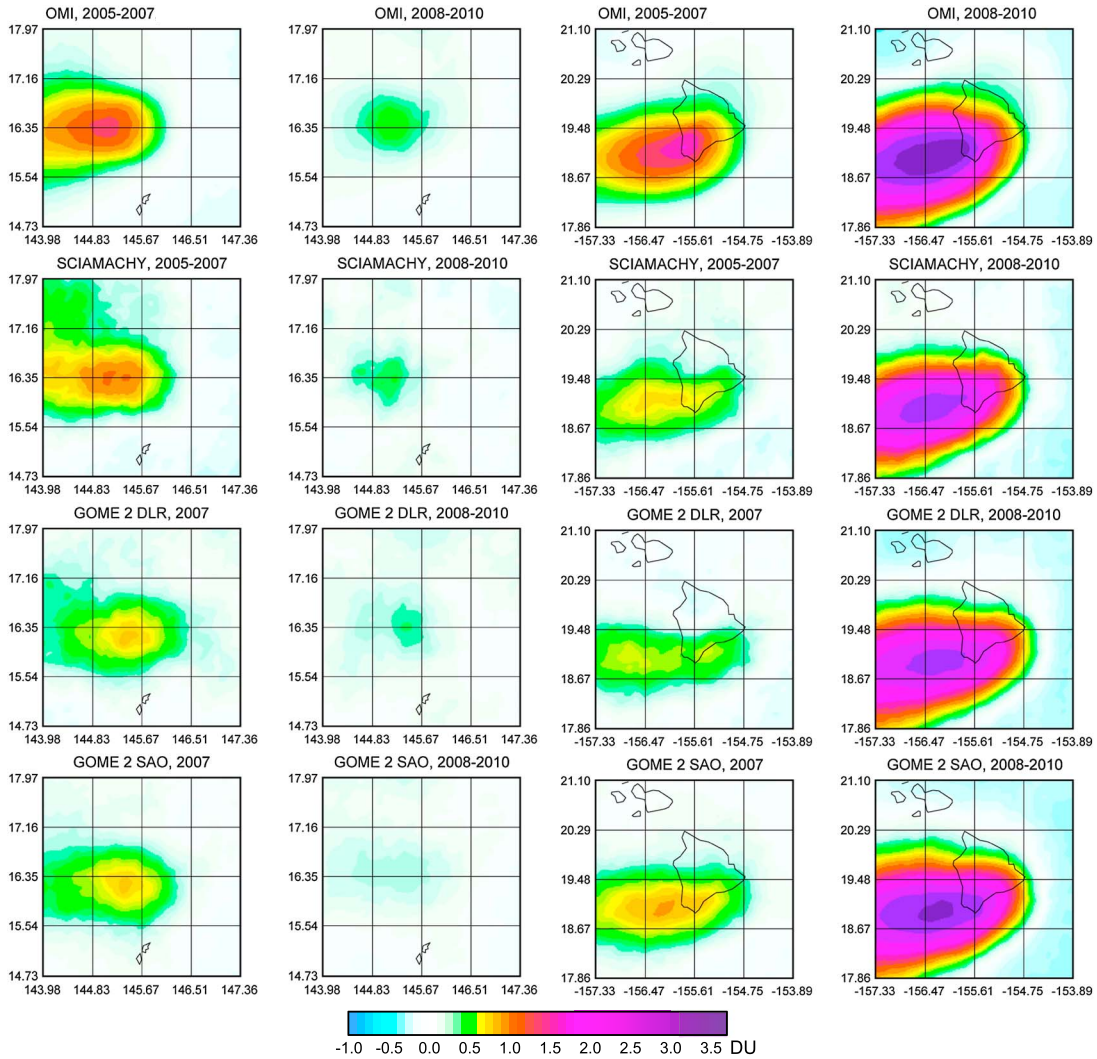


Figure 3. Mean SO₂ distribution over Anatahan and Kilauea volcanoes in DU smoothed using the averaging radius of 60 km for two time intervals. All four data products can successfully track changes in emissions from individual volcanoes. Note that a cutoff limit of 15 DU was used to remove impacts of large eruptions.

a quantity referred to as the signal-to-noise ratio (SNR) and calculated assuming that all measurement errors are independent. Even relatively weak signals in SCIAMACHY and GOME-2 DLR data in 2005–2007 are above the 5-sigma limit, while the SNR is greater than 20 for OMI data. While there could be some correlation between individual measurements, the probability that such an anomaly in the vicinity of a major SO₂ emission source is a random event is negligible. It should also be noted that while both GOME-2 data products are based on the same measurements, SAO shows less scattering and therefore higher SNR than DLR. The lower noise in the GOME-2 SAO product is likely due to the use of a larger fitting window that includes a strong SO₂ spectral feature which peaks near 313 nm.

[27] While all three instruments are able to detect large SO₂ sources, OMI’s better spatial resolution and measurement density gives it an advantage when smaller sources are analyzed or when multiple sources are located in close

proximity. Figure 5 shows 2005–2007 average (winter months excluded) SO₂ values over the eastern U.S. estimated using OMI and SCIAMACHY data as well as the SNR. If the data are smoothed using a 60 km radius, i.e., as in Figures 2 and 3, OMI data show elevated SO₂ levels that are statistically significant. SCIAMACHY data also demonstrated some signs of higher SO₂, albeit with a tenuous SNR. However, when less smoothing is applied, OMI data reveal multiple individual sources in the area (see *Fioletov et al.* [2011] for more information), while SCIAMACHY data become too noisy.

[28] The SNR is governed by the magnitude of the mean values, the number of data points, and the standard deviation of individual SO₂ measurements. The latter is influenced by both instrumental noise, retrieval quality, and SO₂ variability. The larger pixel sizes of SCIAMACHY and GOME-2 instruments (compared to OMI) result in fewer measurements over the same area. It also means that relatively small

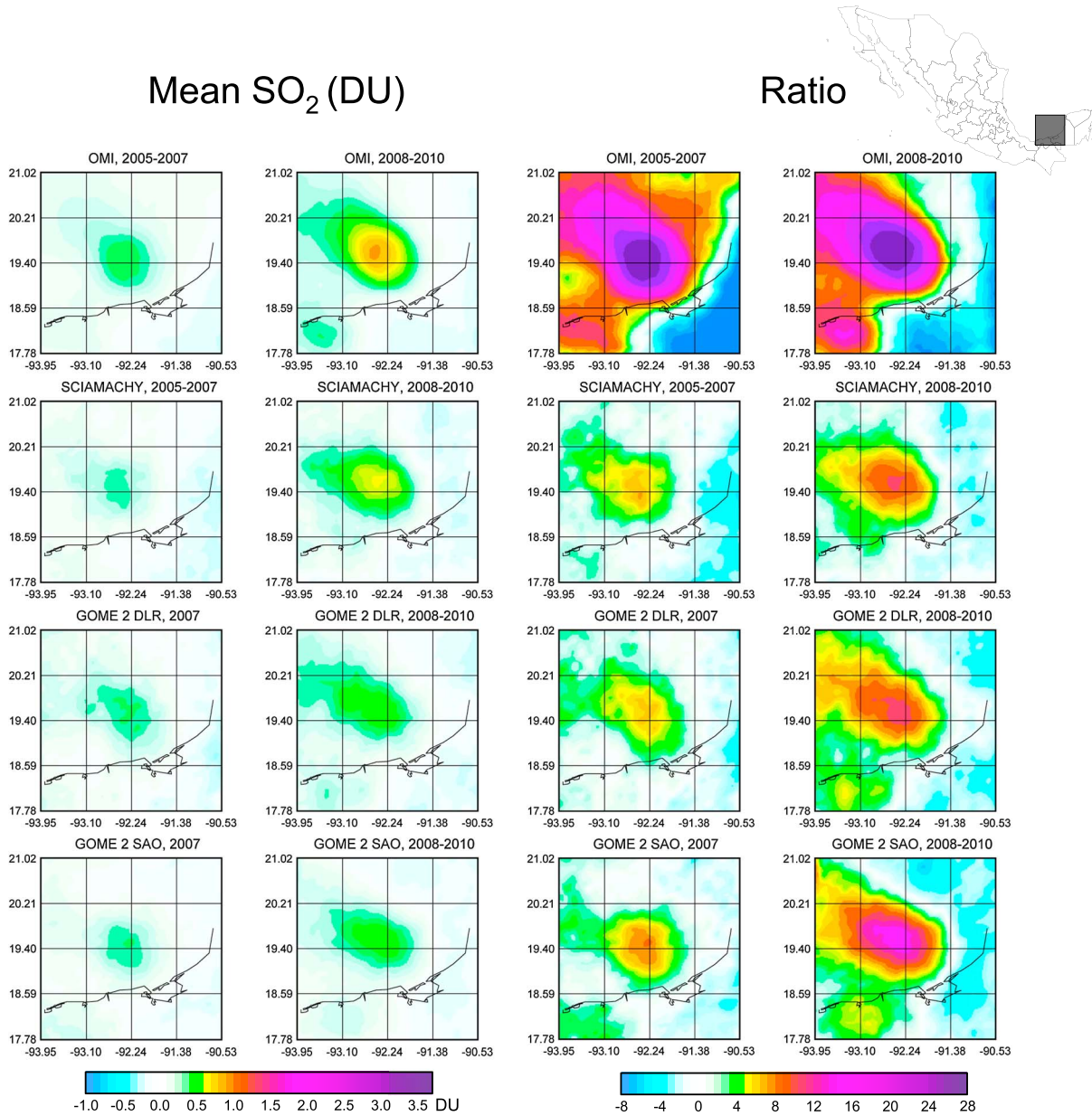


Figure 4. Mean SO₂ distribution over Cantarell and Ku-Maloob-Zaap Oil Fields, Gulf of Mexico, for 2005–2007 and 2008–2010. Data are smoothed using the averaging radius of 60 km. SO₂ values in DU and the ratios between the mean SO₂ and the standard error of the mean are shown.

sources that produce elevated SO₂ values over the area of a few kilometers produce smaller mean values compared to OMI. In the same time, the standard deviations of OMI SO₂ values are even lower than those for the two other instruments. As a result, many sources that are clearly visible from OMI data do not produce a statistically significant SNR in SCIAMACHY and GOME-2 data. As an example, Figure 6 shows SO₂ values over power plants at Megalopolis, Greece, one of the largest SO₂ emission sources in Europe. Annual mean (winter months excluded) values averaged using a 60 km radius are shown. No signal appears in SCIAMACHY and GOME-2 DLR data, while OMI data not only show significantly elevated SO₂ values in the vicinity of the power plants but also demonstrate year-to-year changes in the SO₂ levels (not shown). GOME-2 SAO

data also clearly show significantly elevated values over Megalopolis in 2007 and some indications of elevated values in 2008–2010.

[29] According to the European Pollutant Release and Transfer Register (<http://prtr.ec.europa.eu/>), emissions from Megalopolis were 250 kT yr⁻¹ in 2007 and on average 150 kT yr⁻¹ in 2008–2010. In *Fioletov et al.* [2011] it was demonstrated that sources emitting 70 kT yr⁻¹ can be seen by OMI under optimal conditions. While the source detectability depends on many factors including the number of clear sky days, wind speed, albedo, etc., this example illustrates the difference between OMI and the other two instruments.

[30] A list of natural and anthropogenic SO₂ hot spots identified in each of SCIAMACHY and GOME-2 data products is in Table 1, and the map of their location is shown in

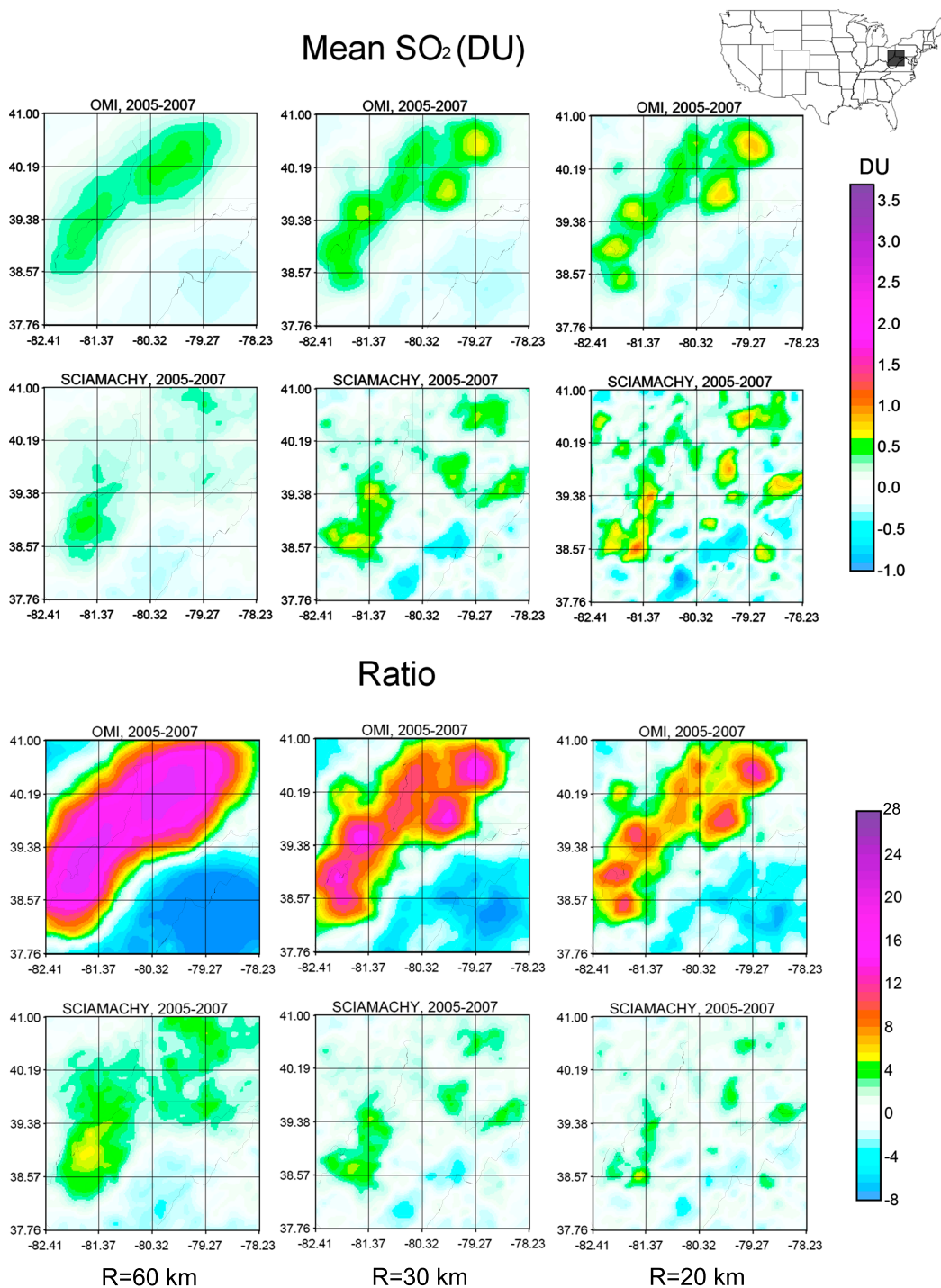


Figure 5. Mean SO₂ over the eastern U.S. from OMI and SCIAMACHY data. (top) SO₂ values in DU and (bottom) the ratios between the mean SO₂ and the standard error of the mean are shown. Calculations were done using 60 km, 30 km, and 20 km averaging radiuses.

Figure 7 with a focus on individual or multiple sources located in close proximity. This list was compiled by first examining global OMI data for 2005–2007 to identify potential hot spots and then determining if they were also detectable in SCIAMACHY and GOME-2 (DLR and SAO) averages above the 5-sigma level. While about 200 locations of elevated SO₂ were identified from OMI data (they are a subject of a separate study), only about 30 of

them produce significant long-term average values from SCIAMACHY and GOME-2 DLR data in either or both of the 2005–2007 and 2008–2010 periods. Explosive volcanic sources that produced high SO₂ levels over a short time, but not in the long-term averages, are not included in Table 1. Also, some of the sources are masked by possible artifacts in satellite data and are not included. While there are many large sources of SO₂ in China, only two clearly

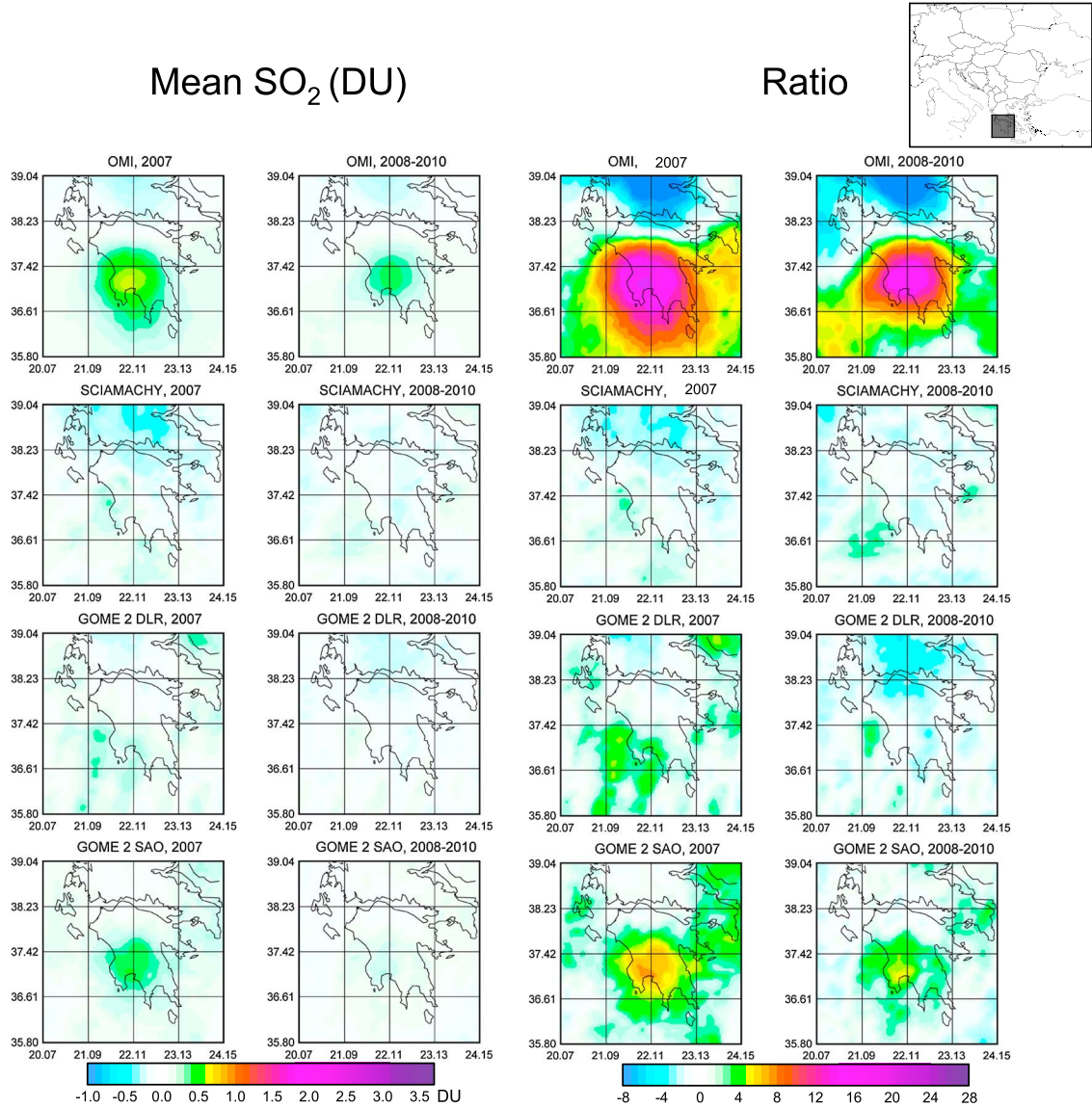


Figure 6. Mean SO₂ distribution over Megalopolis power plants, Greece, in DU. Averages for 2007 and for 2008–2010 are shown. Data are smoothed using the averaging radius of 60 km. (left) SO₂ values in DU and (right) the ratios between the mean SO₂ and the standard error of the mean are shown. No statistically significant signal appears in SCIAMACHY and GOME-2 DLR data, while OMI and GOME-2 SAO data show significantly elevated SO₂ values in the vicinity of the power plants.

meet the criteria above and an analysis of the elevated SO₂ in China on a regional scale is discussed in section 4. Although both SCIAMACHY and GOME-2 (DLR and SAO) data show elevated SO₂ values over the eastern U. S., their resolution is insufficient to identify individual sources (Figure 5) and so they are excluded from Table 1. As Figures 4 and 6 show, GOME-2 SAO data product exhibits a better SNR and therefore there are some sources with long-term averages below the noise level in SCIAMACHY and GOME-2 DLR data sets but above it in GOME-2 SAO data sets. The number of such sources is, however, not very large, about a dozen. Therefore, we focus this study on the sources listed in Table 1, i.e., on those detectable from all four data products.

3.1. Estimation of SO₂ Emissions

[31] An estimate of the annual SO₂ emissions over two periods, 2005–2007 and 2008–2010, was performed for each of the sources listed in Table 1 using a simple mass-balance approach, $E = m/\tau$, where E is the emission rate, m is the SO₂ mass, and τ is the SO₂ removal rate or effective lifetime (resulting from the combination from physical removal and dispersion). The first step involved calculating the steady state, total SO₂ mass (or number of molecules) resulting from that source using the two-dimensional (2-D) Gaussian fitting procedure from *Fioletov et al.* [2011]. All satellite SO₂ measurements (SAT_{SO_2}) within the prescribed time window and radius were fit to $SAT_{SO_2} = a \cdot f(x, y)$ where

$$f(x, y) = \frac{1}{2\pi\sigma_x\sigma_y\sqrt{1-\rho^2}} \exp\left(-\frac{1}{2(1-\rho^2)} \left[\frac{(x-\mu_x)^2}{\sigma_x^2} + \frac{(y-\mu_y)^2}{\sigma_y^2} - \frac{2\rho(x-\mu_x)(y-\mu_y)}{\sigma_x\sigma_y} \right]\right) \quad (1)$$

and x and y refer to the coordinates of the pixel center. Note that individual VCDs and not the smoothed data described in section 3 (and presented in Figures 2–6, for example), were used for the fit. The elliptical shape of the SO₂ distribution near the source is determined by parameters σ_x , σ_y , and ρ . The parameters μ_x and μ_y were included since the position of the fit maximum may be different from the position of the emissions source due to, for example, prevailing winds or if the source is composed of two closely located power plants. Since $\int_{-\infty}^{\infty} \int_{-\infty}^{\infty} f(x, y) dx dy = 1$, the parameter a represents the total observed number of SO₂ molecules near the source. If SAT_{SO₂} is in DU, i.e., in $2.69 \cdot 10^{26}$ molecules km⁻², and σ_x , σ_y are in kilometers, then a is in $2.69 \cdot 10^{26}$ molecules and related to the total mass by $m = a \cdot M/N_A$, where M is molecular weight of SO₂ and N_A is Avogadro's number. The fitting was done using satellite pixels centered within 200 km from the source. This 200 km radius is larger than the 40 and 60 km used by *Fioletov et al.* [2011], as the sources discussed here are larger, and therefore they produce elevated SO₂ levels at greater distances.

[32] Figure 8 shows scatter plots of total amount of SO₂ near the sources from the four satellite data products for 2005–2007 and 2008–2010 periods expressed as total number of molecules. The correlation coefficients between estimates from SCIAMACHY and OMI, GOME-2 DLR and OMI, and GOME-2 SAO and OMI are 0.91, 0.88, and 0.94, respectively, and the slopes of the regression lines are 0.73 ± 0.07 (95% confidence limits), 0.83 ± 0.09 , and 0.91 ± 0.07 , respectively. This shows a good quantitative agreement between SO₂ estimates from the three instruments when local biases are removed. Since the values based on OMI, SCIAMACHY, and GOME-2 data in Figure 8 are in general agreement, they can be considered as independent estimates of total mass that can be averaged to obtain a more accurate emission value.

[33] The mass at each location, averaged over the four products, was converted into an emission rate through an empirical relationship. Using emissions data from the largest U.S. individual sources, *Fioletov et al.* [2011] found a correlation of 0.93 between OMI SO₂ integrated around the source and the annual SO₂ emission rate for the sources

Table 1. List of Continuously Emitting Sources That Are Identifiable in OMI, SCIAMACHY, and GOME-2 SO₂ Data Sets^a

#	Latitude	Longitude	Source Type	Source or Region Name	Country	Emissions 2005–2007	Emissions 2008–2010
1	69.36	88.13	Smelter	Norilsk	Russia	2650 ± 610 ^b	2270 ± 960 ^b
2	46.83	74.94	Smelter	Balqash	Kazakhstan	620 ± 170	650 ± 120
3	44.67	23.41	Power Plants	Rovinary, Turceni, Isalnita	Romania	870 ± 130 ^b	740 ± 130 ^b
4	42.15	25.91	Power Plants	Marica	Bulgaria	600 ± 120	
5	39.44	106.72	Multiple sources	Shizuishan	China	850 ± 410	860 ± 270
6	37.73	15.00	Volcano	Mt. Etna	Italy	940 ± 220 ^b	1020 ± 190 ^b
7	34.08	139.53	Volcano	Miyake-jima	Japan	830 ± 300 ^b	650 ± 260
8	29.98	55.86	Smelter	Sarcheshmeh	Iran	500	450 ± 90
9	29.22	50.32	Oil industry	Khark Island	Iran		
10	23.12	113.25	Multiple sources	Guangdong	China	1830 ± 240	1420 ± 170
11	20.63	39.56	Oil industry	Shoaiba	Saudi Arabia	1830 ± 340	1750 ± 90
12	20.05	-99.28	Industrial and Volcano	Tula, Popocatepetl	Mexico		
13	19.48	-155.61	Volcano	Kilauea, Hawaii	U.S.	1490 ± 510	5850 ± 860
14	19.40	-92.24	Oil industry	Oil fields in Gulf of Mexico	Mexico	530 ± 180 ^b	740 ± 240 ^b
15	19.08	-104.28	Power Plant	Manzanillo	Mexico	640 ± 110	640 ± 110
16	16.72	-62.18	Volcano	Soufrière Hills	Montserrat (UK)	530 ± 150 ^b	570 ± 90 ^b
17	16.35	145.67	Volcano	Anatahan	Northern Mariana Islands	1280 ± 220 ^b	490 ± 90
18	13.26	123.69	Volcano	Mayon	Philippines	680 ± 170	570 ± 240
19	1.68	127.88	Volcano	Dukono	Indonesia	670 ± 180	890 ± 170 ^b
20	-1.41	29.20	Volcano	Nyiragongo	Democratic Republic of Congo	3020 ± 480 ^b	2100 ± 320 ^b
21	-4.08	145.04	Volcano	Manam	Papua New Guinea	1920 ± 640 ^b	990 ± 320
22	-4.12	152.20	Volcano	Turuvurur/Rabaul	Papua New Guinea		
23	-6.09	155.23	Volcano	Bagana	Papua New Guinea	2220 ± 460 ^b	2040 ± 550 ^b
24	-7.94	112.95	Volcano	East Java	Indonesia	2120 ± 390	1930 ± 390 ^b
25	-8.27	123.51	Volcano	Lewotolo	Indonesia	1140 ± 170	850 ± 310
26	-16.25	168.12	Volcano	Ambrym	Vanuatu	3590 ± 390 ^b	4460 ± 460 ^b
27	-17.63	-71.34	Smelter and volcano	Ilo, Ubinas	Peru	3950 ± 430 ^b	1860
28	-26.57	29.17	Power Plants		South Africa	1920 ± 730	1960 ± 790

^aEmission estimated are given in kt(SO₂) per year. Note that fitting is done considering measurements within radius of 200 km and may contain more than one source. If estimates from more than one source are available, the standard deviation of the available estimates is given after the “±” sign.

^bEstimates where reduction of the fitting radius from 200 to 100 km resulted in more than 25% difference in estimated emissions possibly indicating multiple sources.

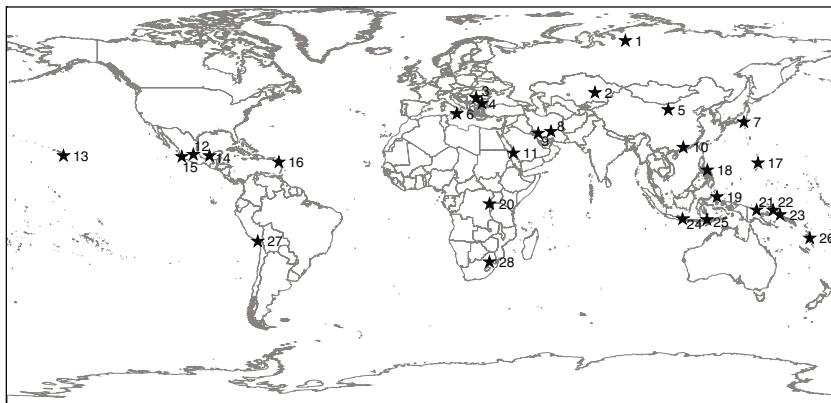


Figure 7. Map of SO₂ sources listed in Table 1.

greater than 70 kT yr^{-1} and suggested a linear relationship between OMI SO₂ integrated around the source and the annual SO₂ emission rate reported by the U.S. power plants. Since the same technique as in *Fioletov et al.* [2011] was used here to calculate SO₂ integrated around the source from satellite data, we applied that linear relationship from *Fioletov et al.* [2011] to estimate the emission rates for all sources listed in Table 1.

[34] Table 1 lists the emission estimates for 2005–2007 and 2008–2010 that provide quantitative characteristics of the changes in SO₂ signals illustrated by Figures 3 and 4. Note that on occasion the nonlinear fit 1 does not always converge, and estimates for some of the sources are missing. This occurs primarily when multiple sources are located within the fitting area. If data from more than one data product produce a reliable fit, estimates for individual data products are averaged and the mean value and the standard deviation are reported in Table 1.

[35] The slope of the used linear emission-mass relation suggested by *Fioletov et al.* [2011] (5 h) can be interpreted as the effective SO₂ summer (May–August) lifetime. A value of $\tau = 5 \text{ h}$ is on the low side as compared to other estimates as, for example, *Lee et al.* [2011] suggested a summer lifetime (not effective) closer to 13 h using the GEOS-CHEM model and about $19 \pm 7 \text{ h}$ from in situ data. Observed SO₂ lifetimes over China were even longer, between 1 and 5 days in the PBL and lower free troposphere. [*Dickerson et al.*, 2007; *He et al.*, 2012; *Li et al.*, 2010a, 2010b]. On the other hand, the *Fioletov et al.* [2011] result is more representative of the true (not effective) in-plume lifetime which can be as short as 2.6 h under scattered clouds [*Zhou et al.*, 2012]. It is important to note that τ estimated with the method presented here indirectly accounts for combined processes of SO₂ dispersion, dry and wet deposition, and chemical conversion to sulfate aerosols, but it does not account for residual SO₂ below satellite detection limit. Thus, it may underestimate integrated SO₂ and, therefore, the estimated lifetime. The results from *Fioletov et al.* [2011] are based on data over the eastern U.S., but, if τ over a particular source differs, this would create an additional error in the emission estimates. This is especially relevant for volcanic sources that emit SO₂ into free troposphere. There are also seasonal and latitudinal variations of τ . Recall, however, that most sources discussed here are located between 30°S and 30°N, and that winter data were excluded from the analysis for the

remaining sites. Thus, for the data analyzed here, it is reasonable to assume that the τ is constant outside winter [see *Lee et al.*, 2011, Figure 2].

[36] It can also be seen from Table 1 that all sources are fairly large, 300 kT yr^{-1} or more. This, in addition to the examples such as Megalopolis, suggests that SCIAMACHY and GOME-2 DLR instruments are able to detect sources that are 4–5 times larger than the 70 kT yr^{-1} limit for sources seen by OMI. Of course, the exact emission levels are subject of more accurate estimates of AMF and τ , but these factors affect OMI, SCIAMACHY, and GOME-2 data in the same way.

[37] An error budget for these emission estimates was constructed, and the results are summarized in Table 2. They are subject to uncertainties from three primary sources. The first is the use of a constant AMF. Monthly SO₂ AMFs from *Lee et al.* [2009], calculated based on vertical profiles from the GEOS-CHEM model [*Bey et al.*, 2001], were sampled at the locations in Table 1 and then averaged to obtain annual values using the same seasonal and solar zenith angle (SZA) criteria as the satellite data. The result is two groupings of AMFs: one of smaller values which reflect locations of elevated a priori SO₂ in the boundary layer and a second group of larger AMFs more representative of background SO₂ profile, suggesting that these are locations for which emissions were underestimated (or zero) in the GEOS-CHEM simulation. The second grouping is made up primarily of volcanic sources but also two to three anthropogenic sources. The average departure of the first grouping from the *Lee et al.* [2009] eastern U.S. summer AMF, which should be representative of all locations, is 25%. This is taken as the variability of the AMFs. There is also an uncertainty in these AMFs from uncertainties in input parameters such as profile shape, surface albedo, cloud fraction, and others. A value of 30% for near-cloud-free conditions is also taken from *Lee et al.* [2009].

[38] The second source of error is from the estimate of the total SO₂ mass as determined from the Gaussian fit. This is quantified considering the statistical uncertainty, which describes how well a 2-D Gaussian model describes the distribution, and the sensitivity of the fit to some of the chosen parameters such as fit radius. The statistical error component is typically 10% for OMI and 25% for the two other instruments. Thus, the combined uncertainty should be no larger than 10%. Also contributing is the chosen fitting

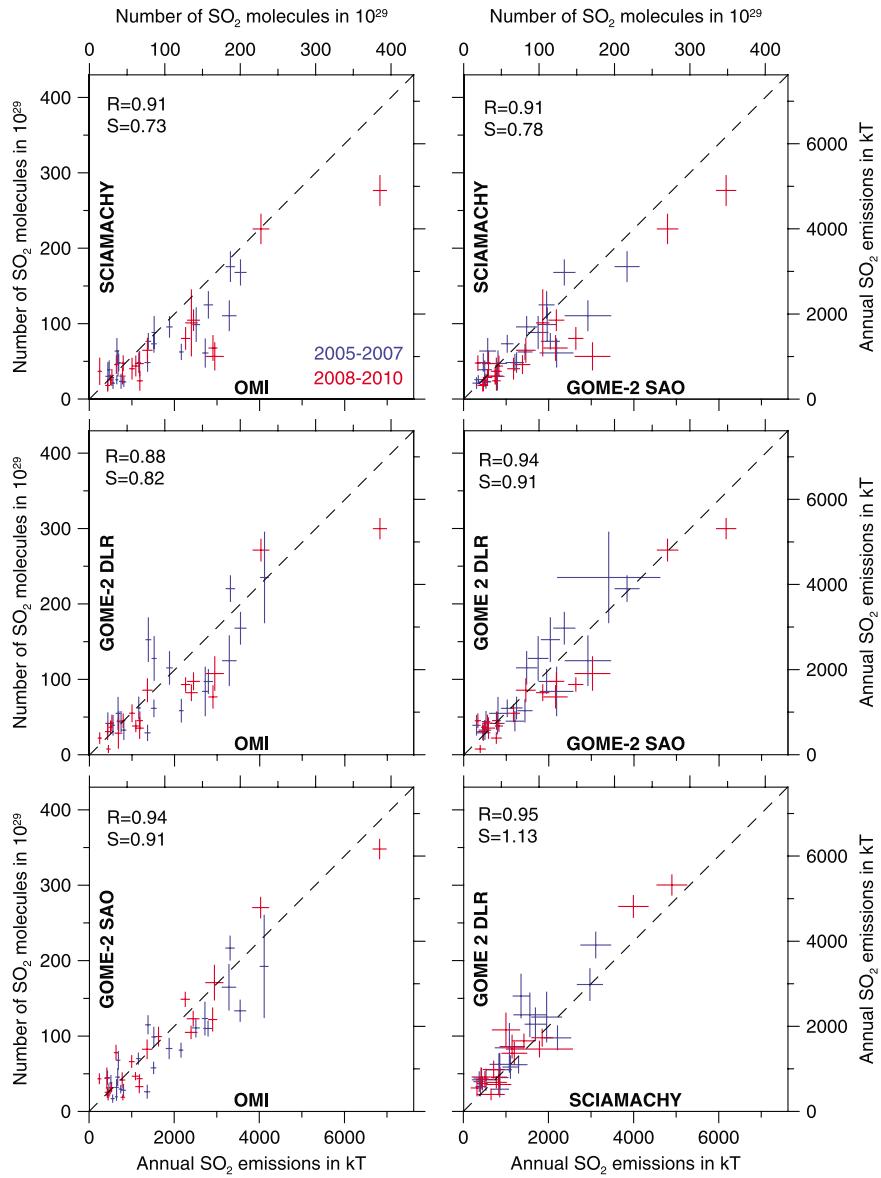


Figure 8. Scatter plots of mean SO₂ integrated near the sources (Table 1 and Figure 7) from OMI, SCIAMACHY, and GOME-2 using the best fit by 2-D Gaussian function. Values on the axis are given in number of molecules and in emission rates estimated for SO₂ effective lifetime of 5 h assuming a constant emission rate throughout the year. The estimates for 2005–2007 (blue) and 2008–2010 (red) are shown. The error bars show the 95% confidence intervals. The correlation coefficient (R) and the slope of the linear fit (S) are shown in the upper left corner of each plot.

Table 2. Uncertainty Budget for Emissions Estimate

Error Category	Source	Magnitude	Note
Slant column density		-	Assumed small due to bias correction and averaging
Air mass factor	Variability	25%	Derived from <i>Lee et al.</i> [2009]
	Uncertainty	30%	Taken from <i>Lee et al.</i> [2009]
Mass	Gaussian fit	10%	Statistical error from Gaussian fit
	Fit radius	25%	From sensitivity study. Could be high if multiple sources
Lifetime	Uncertainty in slope	10%	Estimated from <i>Fioletov et al.</i> [2011]
	Variability	30%	Estimated from <i>Lee et al.</i> [2011]
Total		57%	

radius, R . The 2-D Gaussian fit should not depend on the fitting radius R if R is large enough. The 2-D Gaussian function is intended to describe distribution around a single source. For many locations listed in Table 1, there is more than one source within a 200 km radius of the fitting area, and that may yield an unreliable fit. For some of the very large single sources, elevated SO₂ values are observed even outside of 200 km area, and reduction of the fitting radius yields underestimation of the emissions. The best area for fitting can be determined on a case-by-case basis by removing regions of secondary sources and including the entire area of elevated SO₂ values from primary sources. For this study, however, the primary intent was to show that all four data products produce similar results. Therefore, we included the impact of the selection of the fitting radius as an additional uncertainty factor in Table 2. The mean change in the emission values for sources listed in Table 1 from a reduction of the fitting radius from 200 km to 100 km is 25%. Estimates where such reduction resulted in more than 25% difference are marked by the superscripted b in Table 1.

[39] The final source of uncertainty is from the slope of the linear relationship between integrated SO₂ and emission inventories (which can be interpreted as the SO₂ removal rate). It is important to note that this is the SO₂ removal rate obtained using well-characterized emission inventories and OMI-derived values of SO₂ mass [Fioletov *et al.*, 2011]. Any systematic errors in the determination of SO₂ (including absorption cross-section, aerosols, etc.) would also affect the mass estimates in the same way at the locations of interest in this study and thus tend to cancel. In essence the Fioletov *et al.* [2011] relationship represents a “calibration” of OMI. As a result this uncertainty can be thought of as a combination of the statistical uncertainty of the linear fit, which is small (<10%), and the variability in the SO₂ removal rate among the different locations which is assumed to be primarily a function of latitude and season. The restriction of measurements to SZA of 60° or smaller minimizes the seasonal variation. Using results from Lee *et al.* [2011, Figure 2], a value of 30% seems reasonable. The overall balance of the various error contributions to the uncertainties of estimated emissions is given in Table 2. The uncertainties are rather large, totaling 57%, but mostly systematic, and some of them can be reduced by more accurate model-based AMF estimates or better fitting. There are, however, some sources of uncertainty that are not addressed in Table 2. Parameterization (1) works well for sites where local wind speed is relatively low (with average speed below 5 m/s), but SO₂ is dispersed more rapidly when the wind speed is high and that is not well captured by parameterization (1). It was also assumed that the emissions are constant throughout the year. For example, seasonal variations in emissions and cloud cover can potentially yield a bias in the estimates. However, relative differences in emissions between two time periods at the same location or among difference sources but located at similar conditions should be more reliable.

4. SO₂ Observations Over China

[40] Elevated SO₂ values over China are apparent in satellite data from all four data products (Figure 1), although the absolute values from OMI are very different from these from

SCIAMACHY and GOME-2 (see also Lee *et al.* [2009, Figure 1]). Figure 9 shows maps of SO₂ over major industrial regions of China from all four data sets smoothed by a 60 km radius window for different time intervals. Data for December–February were excluded from the analysis in order to avoid problems related to the difference in zenith angles between the satellites and to the difference in snow albedo. In addition, SO₂ values over China in winter are higher than in other seasons due to longer SO₂ lifetime in winter and possibly due to larger emissions from sources in northern China required for winter heating. SO₂ values over China in spring, summer, and fall are more uniform, and these three seasons were combined together.

[41] The local biases discussed previously are also apparent in Figure 9. For example, negative SO₂ values are seen over eastern Mongolia in OMI data, as is the 0.5 DU step at 30°N over the East China Sea (seen also in Figure 1) related to the change of ozone a priori vertical profiles. SCIAMACHY data show SO₂ values of 0.5–0.7 DU over areas with no known SO₂ sources in Mongolia in 2008–2010 averages, while GOME-2 data show elevated values over the same areas in 2007. Moreover, the highest SO₂ from OMI are only about 70% of that of SCIAMACHY and GOME-2 over the same regions. All of these suggest that some filtering procedure should be applied before comparison of SO₂ values from the three satellites.

[42] The local bias correction described in section 3 is only appropriate for local sources that create elevated SO₂ levels over a limited area and thus can be estimated by averaging data from a “clean” ring located between 250 and 300 km from the source. This is not the case for industrial areas in China, where multiple sources yield high SO₂ levels over vast areas. Therefore, a different approach was used. As before, we assume that the local bias is constant within a circle with radius R . If we also assume that the measurements have no noise, then the lowest value within that area is the best representation of clean conditions and therefore that value can be used as an estimate of the local bias. In the presence of noise, however, the minimum value will be smaller than the local bias and the difference depends on the noise distribution. This provides some direction: the low end of the SO₂ distribution in the area can provide information about the local bias.

[43] The observed values (Z) in the analyzed area can be written in the form $Z = M + X + Y$, where: M is a constant local bias, X is the noise that is normally distributed with known variance σ^2 and zero mean, and Y is the true SO₂ value. We can assume that Y is always positive ($P(Y < 0) = 0$), where P is probability. Also, we can assume that there is a clean “area” $P(Y = 0) = b$, where $b > 0$ but unknown and that X and Y are independent. Instead of the minimum values, the estimates are based on tenth percentiles since they can be estimated more accurately than extreme values. We used $p_{10}(Z) - p_{10}(X)$ as an estimate for M where $p_{10}(X)$ and $p_{10}(Z)$ are the tenth percentiles of X and Z , respectively. If $b = 1$, i.e., $Y \equiv 0$, then the only difference between X and Z distributions is the difference in mean value (0 and M , respectively), i.e., $p_{10}(Z) = p_{10}(X) + M$. If, for example, $b = 0.2$, i.e., there is a clean spot that covers only 20% of the area, and Y is very large otherwise, then $p_{10}(Z) = M$, because the median value over that clean spot corresponds to tenth percentiles of Z . Thus, for the range of b values between

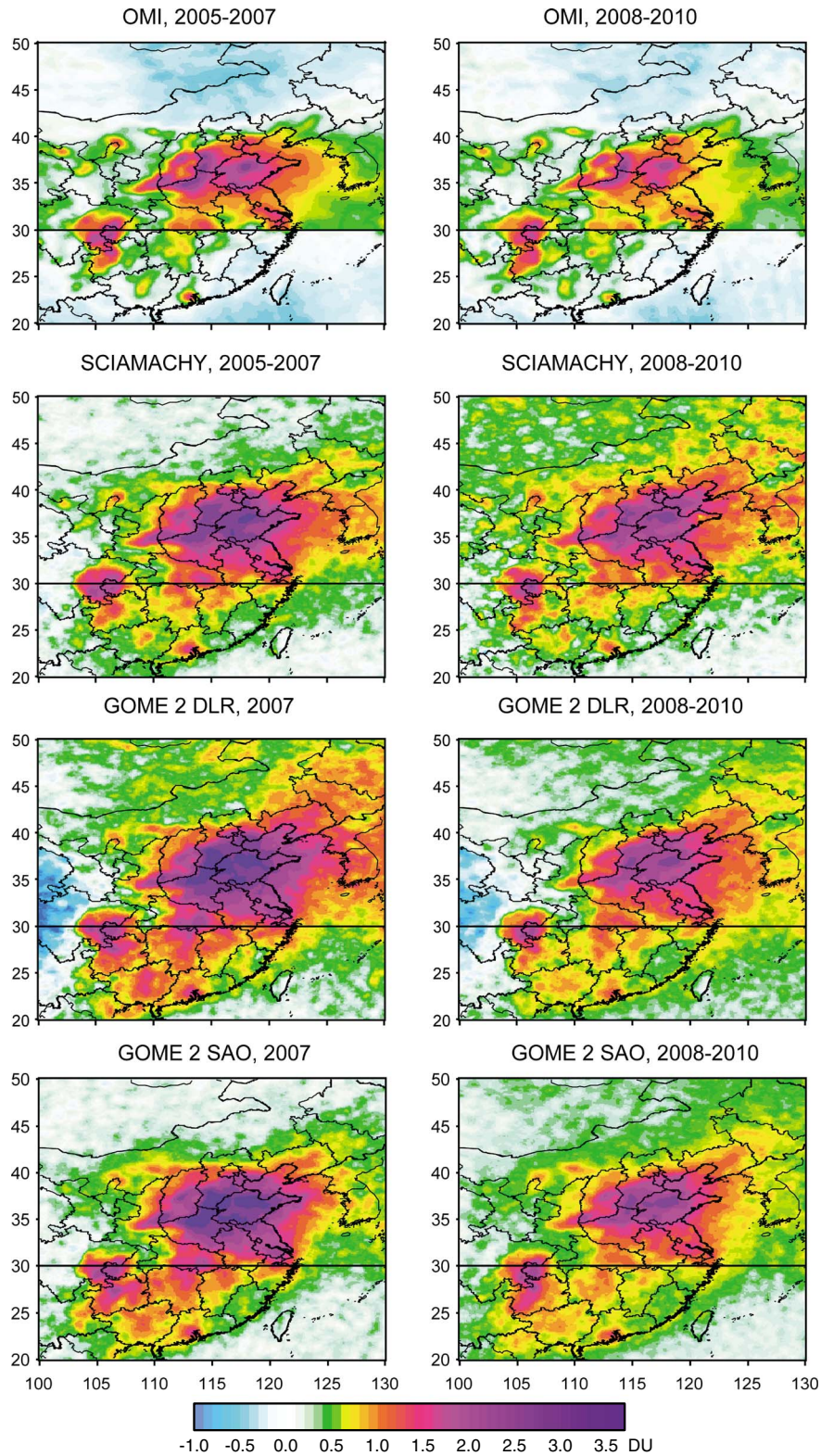


Figure 9. Average SO₂ in DU over major industrial regions of China from OMI, SCIAMACHY, and GOME-2 (DLR and SAO) data smoothed by 60 km radius window for different time intervals. Data for December–February were excluded from the analysis.

0.2 and 1, $p_{10}(Z) - p_{10}(X)$ always lies between M and $M - p_{10}(X)$. For the normal distribution $p_{10}(X) = -1.3\sigma$, that means the accuracy of the estimate of M from Z depends on the standard deviation of X .

[44] Information about the statistical characteristics of X can be obtained from measurements over areas with no SO₂ sources, for example, over the Pacific. All calculations were done on a monthly basis. A 0.1° by 0.1° grid was

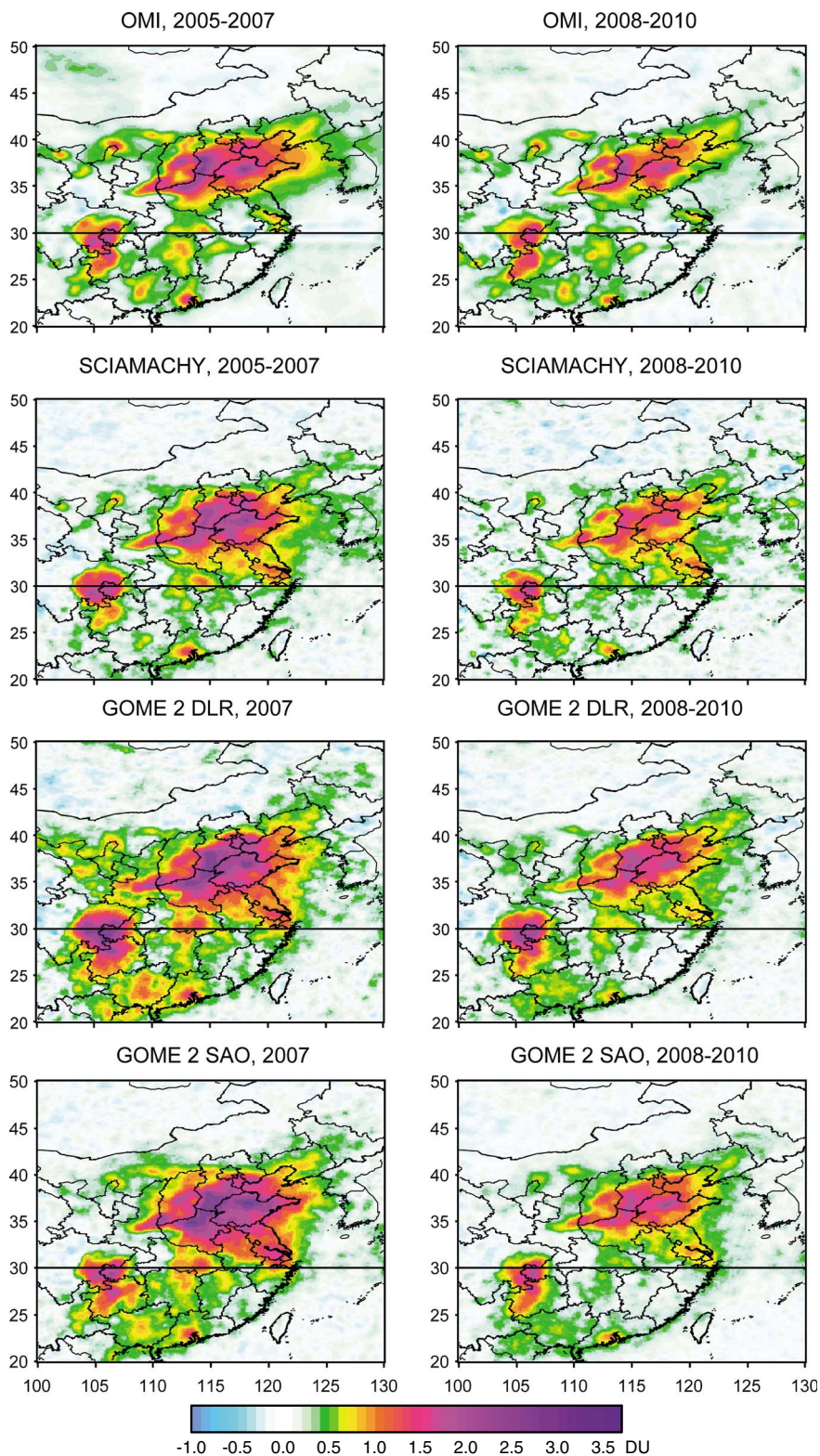


Figure 10. The same as Figure 9, but with the local bias removed by the filtration procedure described in the text.

established, and for each grid point all pixels from a particular month centered within a radius r were averaged. Then, statistical characteristics of the obtained averages were calculated for 5° by 5° cells. Standard deviations calculated for clean cells were used then as values for σ . Values of

σ increase slightly with latitude, and so a linear dependence of σ was assumed. For $r=60$ km (as was used for Figure 9), the values of σ are typically between 0.05 DU and 0.1 DU for OMI and between 0.07 DU and 0.13 DU for the two other instruments. OMI values increased slightly with time

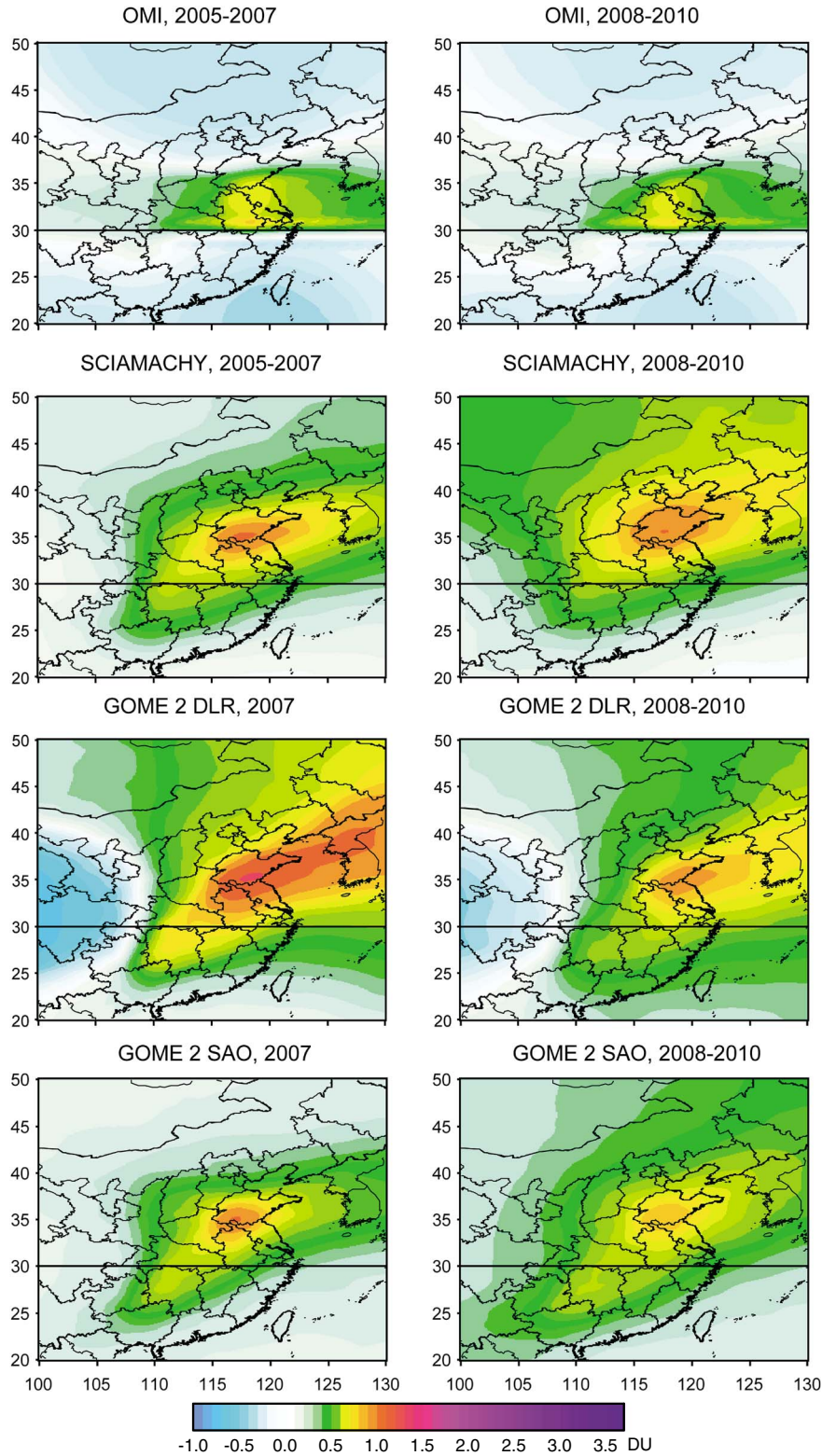


Figure 11. The difference between data shown in Figures 9 and 10, i.e., the estimated local biases in satellite data in DU.

because of reduced sampling due to the row anomaly. Thus, the $p_{10}(X)$ value was typically less than 0.2 DU suggesting the uncertainty in the estimates of M is noticeably less than the 0.5–0.7 DU biases discussed in the beginning of this section.

[45] The value of R needs to be determined in order to apply the suggested filtration procedure. The larger the R value, the more likely that we can find a spot with no SO₂, but then it is less likely that the local bias is indeed uniform within the area. However, R values should not be above

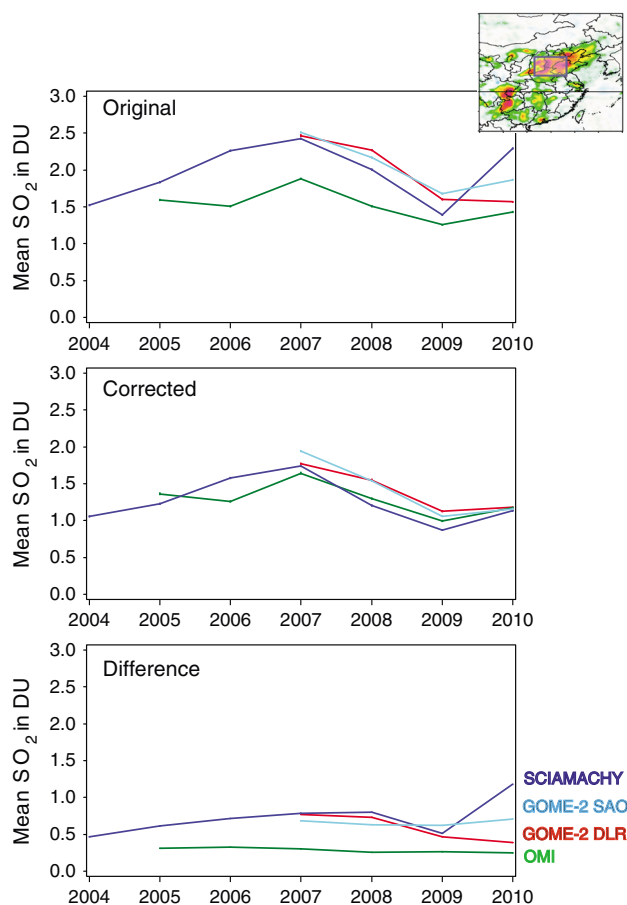


Figure 12. (top) The mean SO₂ values over an area (34°N–38°N, 112°E–118°E) from OMI, SCIAMACHY, and GOME-2 (DLR and SAO), (middle) the mean SO₂ values with local bias removed by the procedure described in the text, and (bottom) the difference between the two panels. Values are given in DU.

~1000 km; otherwise inhomogeneity in ozone distribution could interfere with SO₂ retrievals, thus assuring that bias will vary within R . A value of 700 km was used for Figures 10 and 11. The selection of the parameters for the filtration procedure R , r , as well as the use of tenth percentile are rather subjective, and more validation should be done in order to find the “optimal” values, but as our main goal here is to show that data from different satellite instruments produce similar results if they are processed in the same way, this lies beyond the scope of this work.

[46] The corrected data are shown in Figure 10, and the background values or the difference between the original and corrected data are in Figure 11. The filtration procedure largely removes the differences between the four data products. The corrected data also show a decline in SO₂ between 2005–2008 and 2007–2010 reported in the literature [Li *et al.*, 2010a, 2010b]. This is further illustrated in Figure 12, which shows the annual mean values calculated from all SO₂ measurements (with data filtering applied as described in section 2) over an area (34°N–38°N, 112°E–118°E) with some of the highest SO₂ levels in China. While four data sets show a maximum in 2007, the absolute values are very different, with 1.7 DU from OMI and about 2.5 DU

from SCIAMACHY and GOME-2. This difference is largely caused by difference and variations of background levels. They are relatively small for OMI, but they are as large as 0.7 DU for the two other instruments.

[47] The patterns and absolute levels of the background values (Figure 11) are nearly identical for the two intervals for OMI but different for the three other data products. Large negative values in GOME-2 DLR background values are located in the areas of high elevation (Tibet) and are likely related to the problems in the retrieval algorithm since other satellite data sets do not display the same behavior. The OMI background values (Figure 11) show a clear step change at 30°N related to the change of a priori ozone profiles in the current SO₂ algorithm. If a priori ozone profiles have such large impact on background levels, it can be expected that actual variation in the vertical ozone distribution also affect the retrieved SO₂. China is located in the region of a very strong latitudinal gradient in total ozone, particularly in spring [e.g., Fioletov, 2008], and therefore there is a large variability in the ozone distribution. Difference in the ozone profile sensitivity of the retrieval algorithms between OMI and the two other instruments may explain the observed difference in the background values between them. However, we were not able to establish a link between ozone variations and background SO₂. Figure 11 also shows that significant longitudinal structure exists in these biases, confirming the suspicion from Lee *et al.* [2009] that a simple latitude-based bias correction may be insufficient.

5. Summary and Discussion

[48] Averaging a large number of individual satellite pixels together with a local bias correction (i.e., low and high spatial frequency filtration) was applied to OMI, SCIAMACHY, and GOME-2 satellite SO₂ measurements to detect and study long-term changes in natural and anthropogenic SO₂ sources. About 30 continuously emitting, localized sources, detectable by all three instruments, were found. Some of these sources, e.g., Norilsk, Russia, were previously detected in satellite data; the others, e.g., the oil fields in the Gulf of Mexico, were reported from satellite SO₂ measurements for the first time. Moreover, detailed or recent emission information is not always available for some of these sources. Therefore, their detection and estimate of their emissions represents a significant practical application of satellite SO₂ measurements.

[49] All four data products also demonstrate high regional SO₂ values over industrial regions of China. However these large values are partially caused by local biases. A spatial filtration procedure was developed to separate background SO₂ that is largely artificial from small-scale local SO₂ enhancements caused by pollutions. The observed SO₂ values were then corrected by removal of the background levels. The corrected SO₂ values show very similar patterns and absolute values for all four data products, while the removed background levels and patterns are very different.

[50] The influence of ozone variations of SO₂ retrievals and changes in instrument characteristics cause local biases in the retrieved SO₂ values from satellite instruments. Such local biases persist over vast (on a scale of thousands of kilometers) areas; therefore, great care should be taken before these data are utilized, for example, by assimilation in air

quality forecast models. Even the largest individual sources produce elevated long-term SO₂ values on a local scale of just several tens of kilometers. Therefore, even over regional polluted area with many sources (e.g., eastern China) there will be some relatively clean locations where pollution levels are close to background. This difference in scale between pollution sources and the background can be exploited in order to make use of spatial filtering to isolate and better quantify point sources.

[51] The validity of this approach is demonstrated by the good quantitative agreement between SO₂ estimates from the three instruments when local biases are removed. The correlation coefficients between estimates of total amount of SO₂ near the sources from SCIAMACHY and OMI, GOME-2 DLR and OMI, and GOME-2 SAO and OMI are 0.91, 0.88, and 0.94, respectively, and the slopes of the regression lines are 0.73 ± 0.07 (95% confidence limits), 0.83 ± 0.09 , and 0.91 ± 0.07 , respectively.

[52] A better spatial resolution (i.e., smaller pixel size) and sampling makes OMI better suited for detecting SO₂ sources compared to the two other instruments. While OMI can detect sources that emit 70 kT yr⁻¹ or more, the sensitivity limit of SCIAMACHY and GOME-2 DLR is likely above the 300 kT yr⁻¹ level. Thus, this comparison suggests it is the 4–5 times better spatial resolution that gives OMI this advantage, although other factors such as the signal-to-noise ratio and higher sampling also contribute to a better OMI performance. This further suggests that the Tropospheric Monitoring Instrument (TROPOMI), the next generation of polar-orbiting atmospheric composition instruments (<http://www.tropomi.eu/TROPOMI/Instrument.html>), with pixels size of 7×7 km² at nadir [Veeffkind et al., 2012], i.e., with ~8 times smaller pixel size than that for OMI, should be able to detect sources that emit 10 kT yr⁻¹ or even less, although this would also depend on other instrument characteristics such as the signal-to-noise ratio. This limit could be even lower for future geostationary satellite instruments such as Geostationary Coastal and Air Pollution Events UV imaging spectrometer [Fishman et al., 2012] due to their much more frequent observations. For example, the recently selected geostationary mission, Tropospheric Emissions: Monitoring of Pollution (TEMPO), will take measurements hourly at a spatial resolution of ~ 2.0 km \times 4.5 km at the center of continental U.S. beginning no later than 2020 (<http://www.cfa.harvard.edu/atmosphere/TEMPO/>).

[53] It should be noted that SCIAMACHY and GOME-2 DLR algorithms are largely designed to detect volcanic plumes in near real time, for example, to provide data to the Support to Aviation Control Service (SACS) hosted by the Belgian Institute for Space Aeronomy (<http://sacs.aeronomie.be>). The more complex and sophisticated but computationally expensive GOME-2 SAO algorithm processes data “off-line.” It has a better SNR than GOME-2 DLR and therefore suggests the smaller SO₂ emission sources can be monitored. Nevertheless, the majority of individual sources detectable from OMI data are below the detectability limit when GOME-2 SAO data product is used. It is also expected that more sophisticated algorithms [Yang et al., 2010] can be used to process OMI data in the future that can further improve the SO₂ emission monitoring capabilities of the OMI instrument.

[54] **Acknowledgments.** We acknowledge the NASA Earth Science Division for funding of OMI SO₂ product development and analysis. The

Dutch-Finnish-built OMI instrument is part of the NASA EOS Aura satellite payload. The OMI project is managed by KNMI and the Netherlands Agency for Aerospace Programs (NIVR). The generation of the GOME-2 SO₂ operational products has been funded by the O3M-SAF project with EUMETSAT and national contributions. The SCIAMACHY data product has been developed under ESA funding within the TEMIS, SACS, and GSE PROMOTE projects. The work of one of the coauthors (C.L.) was supported by the Advanced Research on Applied Meteorology of the Korea Meteorological Administration (KMA).

References

- Aquino, J. A. L., J. M. Ruiz, M. A. F. Flores, and J. H. García (2005), The Sihli field: Another giant below Cantarell, offshore Campeche, Mexico, *AAPG Mem.*, *78*, 141–150.
- Beirle, S., U. Platt, R. von Glasow, M. Wenig, and T. Wagner (2004), Estimate of nitrogen oxide emissions from shipping by satellite remote sensing, *Geophys. Res. Lett.*, *31*, L18102, doi:10.1029/2004GL020312.
- Bey, I., D. J. Jacob, R. M. Yantosca, J. A. Logan, B. D. Field, A. M. Fiore, Q. Li, H. Y. Liu, L. J. Mickley, and M. G. Schultz (2001), Global modeling of tropospheric chemistry with assimilated meteorology: Model description and evaluation, *J. Geophys. Res.*, *106*(D19), 23,073–23,095, doi:10.1029/2001JD000807.
- Bovensmann, H., J. P. Burrows, M. Buchwitz, J. Frerick, S. Noël, V. V. Rozanov, K. V. Chance, and A. H. P. Goede (1999), SCIAMACHY—Mission objectives and measurement modes, *J. Atmos. Sci.*, *56*(2), 127–150.
- Callies, J., E. Corpaccioli, M. Eisinger, A. Hahne, and A. Lefebvre (2000), GOME-2—MetOp’s second generation sensor for operational ozone monitoring, *ESA Bull.*, *102*, 28–36.
- Carn, S. A., A. J. Krueger, G. J. S. Bluth, S. J. Schaefer, N. A. Krotkov, I. M. Watson, and S. Datta (2003), Volcanic eruption detection by the Total Ozone Mapping Spectrometer (TOMS) instruments: A 22-year record of sulphur dioxide and ash emissions, in *Volcanic Degassing*, vol. 213, edited by C. Oppenheimer, D. M. Pyle, and J. Barclay, pp. 177–202, Spec. Publ. Geol. Soc., London.
- Carn, S. A., A. J. Krueger, N. A. Krotkov, K. Yang, and P. F. Levelt (2007), Sulfur dioxide emissions from Peruvian copper smelters detected by the Ozone Monitoring Instrument, *Geophys. Res. Lett.*, *34*, L09801, doi:10.1029/2006GL029020.
- Clarisse, L., M. Fromm, Y. Ngadi, L. Emmons, C. Clerbaux, D. Hurtmans, and P. F. Coheur (2011), Intercontinental transport of anthropogenic sulfur dioxide and other pollutants: An infrared remote sensing case study, *Geophys. Res. Lett.*, *38*, L19806, doi:10.1029/2011GL048976.
- Clarisse, L., D. Hurtmans, C. Clerbaux, J. Hadji-Lazaro, Y. Ngadi, and P.-F. Coheur (2012), Retrieval of sulphur dioxide from the infrared atmospheric sounding interferometer (IASI), *Atmos. Meas. Tech.*, *5*, 581–594, doi:10.5194/amt-5-581-2012.
- de Foy, B., N. A. Krotkov, N. Bei, S. C. Herndon, L. G. Huey, A.-P. Martínez, L. G. Ruiz-Suárez, E. C. Wood, M. Zavala, and L. T. Molina (2009), Hit from both sides: Tracking industrial and volcanic plumes in Mexico City with surface measurements and OMI SO₂ retrievals during the MILAGRO field campaign, *Atmos. Chem. Phys.*, *9*(24), 9,599–9,617.
- Dickerson, R. R., et al. (2007), Aircraft observations of dust and pollutants over northeast China: Insight into the meteorological mechanisms of transport, *J. Geophys. Res.*, *112*, D24S90, doi:10.1029/2007JD008999.
- Eisinger, M., and J. P. Burrows (1998), Tropospheric sulfur dioxide observed by the ERS-2 GOME instrument, *Geophys. Res. Lett.*, *25*(22), 4,177–4,180.
- Feller, G. (2012), Mexico strives to increase output, *World Oil*, *233*, 81.
- Fioletov, V. E. (2008), Ozone climatology, trends, and substances that control ozone, *Atmos. Ocean*, *46*, 39–67, doi:10.3137/ao.460103.
- Fioletov, V. E., C. A. McLinden, N. Krotkov, M. D. Moran, and K. Yang (2011), Estimation of SO₂ emissions using OMI retrievals, *Geophys. Res. Lett.*, *38*, L21811, doi:10.1029/2011GL049402.
- Fishman, J., et al. (2012), The United States’ next generation of atmospheric composition and coastal ecosystem measurements: NASA’s Geostationary Coastal and Air Pollution Events (GEO-CAPE) Mission (2011), *Bull. Am. Meteorol. Soc.*, *93*(10), 1,547–1,566, doi:10.1175/BAMS-D-11-00201.1.
- Georgoulas, A. K., D. Balis, M. E. Koukouli, C. Meleti, A. Bais, and C. Zerefos (2009), A study of the total atmospheric sulfur dioxide load using ground-based measurements and the satellite derived Sulfur Dioxide Index, *Atmos. Environ.*, *43*, 1693–1701.
- He, H., et al. (2012), SO₂ over central China: Measurements, numerical simulations and the tropospheric sulfur budget, *J. Geophys. Res.*, *117*, D00K37, doi:10.1029/2011JD016473.
- Heald, C. L., D. J. Jacob, R. J. Park, B. Alexander, T. D. Fairlie, R. M. Yantosca, and D. A. Chu (2006), Transpacific transport of Asian anthropogenic aerosols and its impact on surface air quality in the United States, *J. Geophys. Res.*, *111*, D14310, doi:10.1029/2005JD006847.

- Hutchinson, T. C., and L. M. Whitby (1977), The effects of acid rainfall and heavy metal particulates on a boreal Forest ecosystem near the Sudbury smelting region of Canada, *Water Air Soil Pollut.*, **7**, 421–438.
- Intergovernmental Panel on Climate Change (2001), *Climate Change 2001: The Scientific Basis*, 881 pp., Cambridge Univ. Press, Cambridge, U. K.
- Janssens-Maenhout, G., A. M. R. Petrescu, M. Muntean, and V. Blujdea (2011), Verifying greenhouse gas emissions: Methods to support international climate agreements, *Greenh. Gas Meas. Manage.*, **1**, 132–133, doi:10.1080/20430779.2011.579358.
- Jiang, J., Y. Zha, J. Gao, and J. Jiang (2012), Monitoring of SO₂ column concentration change over China from Aura OMI data, *Int. J. Remote Sens.*, **33**(6), 1934–1942.
- Karagulian, F., L. Clarisse, C. Clerbaux, A. J. Prata, D. Hurtmans, and P. F. Coheur (2010), Detection of volcanic SO₂, ash, and H₂SO₄ using the Infrared Atmospheric Sounding Interferometer (IASI), *J. Geophys. Res.*, **115**, D00L02, doi:10.1029/2009JD012786.
- Krotkov, N. A., S. A. Carn, A. J. Krueger, P. K. Bhartia, and K. Yang (2006), Band residual difference algorithm for retrieval of SO₂ from the Aura Ozone Monitoring Instrument (OMI), *IEEE Trans. Geosci. Remote Sens.*, **44**, 1259–1266.
- Krotkov, N. A., et al. (2008), Validation of SO₂ retrievals from the Ozone Monitoring Instrument over NE China, *J. Geophys. Res.*, **113**, D16S40, doi:10.1029/2007JD008818.
- Krueger, A. J., S. J. Schaefer, N. Krotkov, G. Bluth, and S. Barker (2000), Ultraviolet remote sensing of volcanic emissions, in *Remote Sensing of Active Volcanism*, Geophys. Monogr. Ser., vol. 116, edited by P. J. Mouginis-Mark, J. A. Crisp, and J. H. Fink, pp. 25–43, AGU, Washington, D. C., doi:10.1029/GM116p0025.
- Lee, C., A. Richter, M. Weber, and J. P. Burrows (2008), SO₂ retrieval from SCIAMACHY using the Weighting Function DOAS (WFDOAS) technique: Comparison with standard DOAS retrieval, *Atmos. Chem. Phys.*, **8**, 6,137–6,145, doi:10.5194/acp-8-6137-2008.
- Lee, C., R. V. Martin, A. van Donkelaar, G. O’Byrne, N. Krotkov, A. Richter, L. G. Huey, and J. S. Holloway (2009), Retrieval of vertical columns of sulfur dioxide from SCIAMACHY and OMI: Air mass factor algorithm development, validation, and error analysis, *J. Geophys. Res.*, **114**, D22303, doi:10.1029/2009JD012123.
- Lee, C., R. V. Martin, A. van Donkelaar, H. Lee, R. Dickerson, J. C. Hains, N. A. Krotkov, A. Richter, K. Vinnikov, and J. J. Schwab (2011), SO₂ emissions and lifetimes: Estimates from inverse modeling using in situ and global, space-based (SCIAMACHY and OMI) observations, *J. Geophys. Res.*, **116**, D06304, doi:10.1029/2010JD014758.
- Levelt, P. F., G. H. J. van den Oord, M. R. Dobber, A. Mäkkki, H. Visser, J. de Vries, P. Stammes, P. Lundell, and H. Saari (2006), The Ozone Monitoring Instrument, *IEEE Trans. Geosci. Remote Sens.*, **44**(5), 1,093–1,101, doi:10.1109/TGRS.2006.872333.
- Li, C., Q. Zhang, N. A. Krotkov, D. G. Streets, K. He, S.-C. Tsay, and J. F. Gleason (2010a), Recent large reduction in sulfur dioxide emissions from Chinese power plants observed by the Ozone Monitoring Instrument, *Geophys. Res. Lett.*, **37**, L08807, doi:10.1029/2010GL042594.
- Li, C., N. A. Krotkov, R. R. Dickerson, Z. Li, K. Yang, and M. Chin (2010b), Transport and evolution of a pollution plume from northern China: A satellite-based case study, *J. Geophys. Res.*, **115**, D00K03, doi:10.1029/2009JD012245.
- Liu, G., D. W. Tarasick, V. E. Fioletov, C. E. Sioris, and Y. J. Rochon (2009), Ozone correlation lengths and measurement uncertainties from analysis of historical ozonesonde data in North America and Europe, *J. Geophys. Res.*, **114**, D04112, doi:10.1029/2008JD010576.
- Longo, B. M., W. Yang, J. B. Green, F. L. Crosby, and V. L. Crosby (2010), Acute health effects associated with exposure to volcanic air pollution (VOG) from increased activity at Kilauea volcano in 2008, *J. Toxicol. Environ. Health*, **73**, 1370–1381.
- McLinden, C. A., V. Fioletov, K. F. Boersma, N. Krotkov, C. E. Sioris, J. P. Veefkind, and K. Yang (2012), Air quality over the Canadian oil sands: A first assessment using satellite observations, *Geophys. Res. Lett.*, **39**, L04804, doi:10.1029/2011GL050273.
- Norilsk Nickel (2009), Annual Report 2009, OJSC MMC Norilsk Nickel, 27 May 2010 Resolution № FMK/20-np-cd, available online at <http://www.norilsk.ru/en/investor/report/annual/>.
- Nowlan, C. R., X. Liu, K. Chance, Z. Cai, T. P. Kurosu, C. Lee, and R. V. Martin (2011), Retrievals of sulfur dioxide from the Global Ozone Monitoring Experiment 2 (GOME-2) using an optimal estimation approach: Algorithm and initial validation, *J. Geophys. Res.*, **116**, D18301, doi:10.1029/2011JD015808.
- Park, R. J., Jacob, D. J., Field, B. D., and Yantosca, R. M. (2004), Natural and transboundary pollution influences on sulphate-nitrate ammonium aerosols in the United States: Implications for policy, *J. Geophys. Res.*, **109**, D15204, doi:10.1029/2003JD004473.
- Platt, U. (1994), Differential optical absorption spectroscopy (DOAS), in *Air Monitoring by Spectroscopic Techniques*, Chem. Anal. Ser., vol. 127, pp. 27–84, John Wiley, New York.
- Pope, C. A., III, and D. W. Dockery (2006), Health effects of fine particulate air pollution: Lines that connect, *J. Air Waste Manage. Assoc.*, **56**, 709–742.
- Rix, M., P. Valks, N. Hao, D. Loyola, H. Schlager, H. Huntrieser, J. Flemming, U. Koehler, U. Schumann, and A. Inness (2012), Volcanic SO₂, BrO and plume height estimations using GOME-2 satellite measurements during the eruption of Eyjafjallajökull in May 2010, *J. Geophys. Res.*, **117**, D00U19, doi:10.1029/2011JD016718.
- Schoeberl, M. R., et al. (2006), Overview of the EOS Aura Mission, *IEEE Trans. Geosci. Rem. Sens.*, **44**(5), 1,066–1,074, doi:10.1109/TGRS.2005.861950.
- Streets, D. G., and S. T. Waldhoff (2000), Present and future emissions of air pollutants in China: SO₂, NO_x and CO, *Atmos. Environ.*, **34**, 363–374.
- Streets, D. G., et al. (2013), Emissions estimation from satellite retrievals: A review of current capability, *Atmos. Environ.*, **77**, 1011–1042.
- Talwani, M. (2011), The future of oil in Mexico, *The James A. Baker III Institute for Public Policy of Rice University*, 34 pp., <http://bakerinstitute.org/publications/EF-pub-TalwaniGeology-04292011.pdf>
- Theys, N., J. van Gent, M. Van Roozendaal, M. Koukouli, D. Balis, P. Hedelt, and P. Valks (2013), Interim verification report of GOME-2 GDP 4.7 SO₂ column data for MetOp-B, *SAF/O3M/IASB/VR/SO2/112*, available at: <http://o3msaf.fmi.fi>.
- Thomas, W., T. Erbertseder, T. Ruppert, M. Van Roozendaal, J. Verdebout, D. Balis, C. Meleti, and C. Zerefos (2005), On the retrieval of volcanic sulfur dioxide emissions from GOME backscatter measurements, *J. Atmos. Chem.*, **50**, 295–320.
- Valdés-Manzanilla, A., G. Fernández-García, S. Ramos-Herrera, and R. G. Bautista-Margulis (2008), Simulación de la concentración de SO₂ emitido por fuentes fijas mayores durante 2003 en el noroeste de Chiapas y centro de Tabasco, México, *Rev. Int. Contam. Ambiental*, **24**, 71–77.
- Valks, P., and D. Loyola (2008), Algorithm Theoretical Basis Document for GOME-2 Total Column Products of Ozone, Minor Trace Gases and Cloud Properties (GDP 4.2 for O3M-SAF OTO and NTO), *DLR/GOME-2/ATBD/01, Iss./Rev.: 1/D*, 26 September 2008, Available online at: <http://wdc.dlr.de/sensors/gome2>.
- vanDonkelaar, A., et al. (2008), Analysis of aircraft and satellite measurements from the Intercontinental Chemical Transport Experiment (INTEX-B) to quantify long-range transport of East Asian sulfur to Canada, *Atmos. Chem. Phys.*, **8**(11), 2,999–3,014, doi:10.5194/acp-8-2999-2008.
- Veefkind, J. P., et al. (2012), TROPOMI on the ESA Sentinel-5 Precursor: A GMES mission for global observations of the atmospheric composition for climate, air quality and ozone layer applications, *Remote Sens. Environ.*, **120**, 70–83.
- Villasenor, R., et al. (2003), An air quality emission inventory of offshore operations for the exploration and production of petroleum by the Mexican oil industry, *Atmos. Environ.*, **37**, 3,713–3,729, doi:10.1016/S1352-2310(03)00445-X.
- Walter, D., K.-P. Heue, A. Rauthe-Schöch, C. A. M. Brenninkmeijer, L. N. Lamsal, N. A. Krotkov, and U. Platt (2012), Flux calculation using CARIBIC DOAS aircraft measurements: SO₂ emission of Norilsk, *J. Geophys. Res.*, **117**, D11305, doi:10.1029/2011JD017335.
- Witte, J. C., M. R. Schoeberl, A. R. Douglass, J. F. Gleason, N. A. Krotkov, J. C. Gille, K. E. Pickering, and N. Livesey (2009), Satellite observations of changes in air quality during the 2008 Beijing Olympics and Paralympics, *Geophys. Res. Lett.*, **36**, L17803, doi:10.1029/2009GL039236.
- Yang, K., N. A. Krotkov, A. J. Krueger, S. A. Carn, P. K. Bhartia, and P. F. Levelt (2007), Retrieval of large volcanic SO₂ columns from the Aura Ozone Monitoring Instrument: Comparison and limitations, *J. Geophys. Res.*, **112**, D24S43, doi:10.1029/2007JD008825.
- Yang, K., X. Liu, P. K. Bhartia, N. A. Krotkov, S. A. Carn, E. J. Hughes, A. J. Krueger, R. J. D. Spurr, and S. G. Trahan (2010), Direct retrieval of sulfur dioxide amount and altitude from spaceborne hyperspectral UV measurements: Theory and application, *J. Geophys. Res.*, **115**, D00L09, doi:10.1029/2010JD013982.
- Zhang, Q., K. He, and H. Huo (2012), Cleaning China’s air, *Nature*, **484**, 161–162.
- Zhou, W., D. S. Cohan, R. W. Pinder, J. A. Neuman, J. S. Holloway, J. Peischl, T. B. Ryerson, J. B. Nowak, F. Flocke, and W. G. Zheng (2012), Observation and modeling of the evolution of Texas power plant plumes, *Atmos. Chem. Phys.*, **12**, 455–468.